9. JOINING

A. Forming Limits of Weld Metal in Aluminum Alloys and Advanced High-Strength Steels

Principal Investigator: Richard W. Davies
Pacific Northwest National Laboratory (PNNL)
P.O. Box 999, Richland, WA 99352-0999
(509) 375-6474; fax: (509) 375-5994; e-mail: rich.davies@pnl.gov

Technology Area Development Manager: Joseph A. Carpenter
(202) 586-1022; fax: (202) 586-1600; e-mail: joseph.carpenter@ee.doe.gov

Expert Technical Monitor: Philip S. Sklad
(865) 574-5069; fax: (865) 576-4963; e-mail: skladps@ornl.gov

Participants:
Elizabeth V. Stephens and Glenn J. Grant, PNNL
General Motors, Chrysler, Ford, US Steel, Alcoa

Contractor: PNNL
Contract No.: DE-AC06-76RL01830

Objective

- Develop, validate, and disseminate a combined experimental and numerical method to statistically describe and systematically quantify the forming limits of welded aluminum (Al) alloys and advanced high-strength steels (AHSSs).

Approach

- Develop a standard tool for weld-process development that will systematically quantify failure probabilities during forming.
- Provide accurate and standardized methods of experimentally characterizing weld-metal formability using unique, but simple, test methods available on the shop floor.
- Provide predictive models for more accurate forming simulations of tailor-welded blanks (TWBs) and hydroforming operations. Predict parts-per-thousand failure rates during production from finite-element analysis (FEA).
- Characterize static/fatigue properties and forming behavior of several weld populations and correlate with statistically-based tool.

Accomplishments

- Completed uniaxial experiments of friction-stir welded (FSW) AA5182-O material population.
- Increased focus on biaxial forming experiments of FSW AA5182-O to 6111-T4 material population.
- Completed coordinate transformations (utilizing digital-imaging correlation) of full-dome biaxial tests of laser-welded (LW) DP 600 and AA5182-6111 welded alloy populations to improve accuracy of strain results input into the model.
- Completed all biaxial experiments for each welded alloy population.
- Completed the combined forming-limit prediction for DP 600, AA5182-6111, and AA5182 welded alloys.

- Participated in the Minerals, Metals, and Materials Society (TMS) 2007 Annual Meeting and presented two presentations related to project work.
- Participated in Materials Science and Technology (MS&T) 2007 Conference and Exhibition and presented one presentation related to project work.

Future Direction

- Quantify the combined forming-limit diagram (FLD) using the statistical approach for each welded alloy population.
- With original equipment manufacturer (OEM) participation, validate the experimental and numerical methodology with any existing TWB applications in production.
- Complete all final work and submit journal articles detailing work and findings.
- Conduct final project presentation summarizing results with Industrial Team Advisory Committee.

Introduction

This work is a collaborative effort between PNNL, the United States (U.S.) Automotive Materials Partnership (USAMP) team of the U. S. Council for Automotive Research (USCAR), U.S. Steel, Olympic Controls, and Alcoa. This project will develop, validate, and disseminate combined experimental and numerical methods that systematically quantify the forming limits of weld materials in Al alloys and AHSSs through a combination of experimental and deformation-modeling analysis. This work will enable high-volume, robust deployment of TWB, seam-welded tubes and tailor-welded tubes in emerging materials. Figure 1 is a schematic of the project.

The deformation of weld materials and their limits of formability are important aspects to both TWB and hydroforming technologies. The conventional, low-carbon steels used in automotive applications are easily fusion welded using conventional technologies and suffer no appreciable strength degradation near the weld. Al alloys are more difficult to weld than low-carbon steels due to high conductivity and reflectivity and low molten viscosity. Al also has a high propensity for porosity to form during fusion welding as well as hot cracking and heat-affected zone (HAZ) related issues in heat-treatable Al alloys. Many of the AHSSs that are finding increasing application in the automotive industry suffer from degradation of strength in the HAZ. Furthermore, nearly all

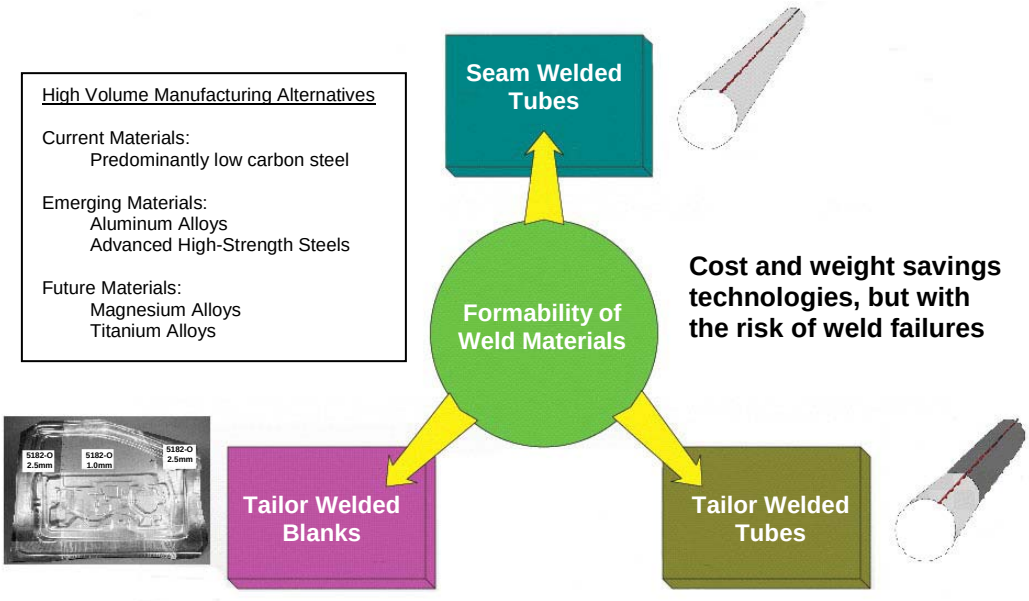

Figure 1. A schematic of the formability of weld materials project.

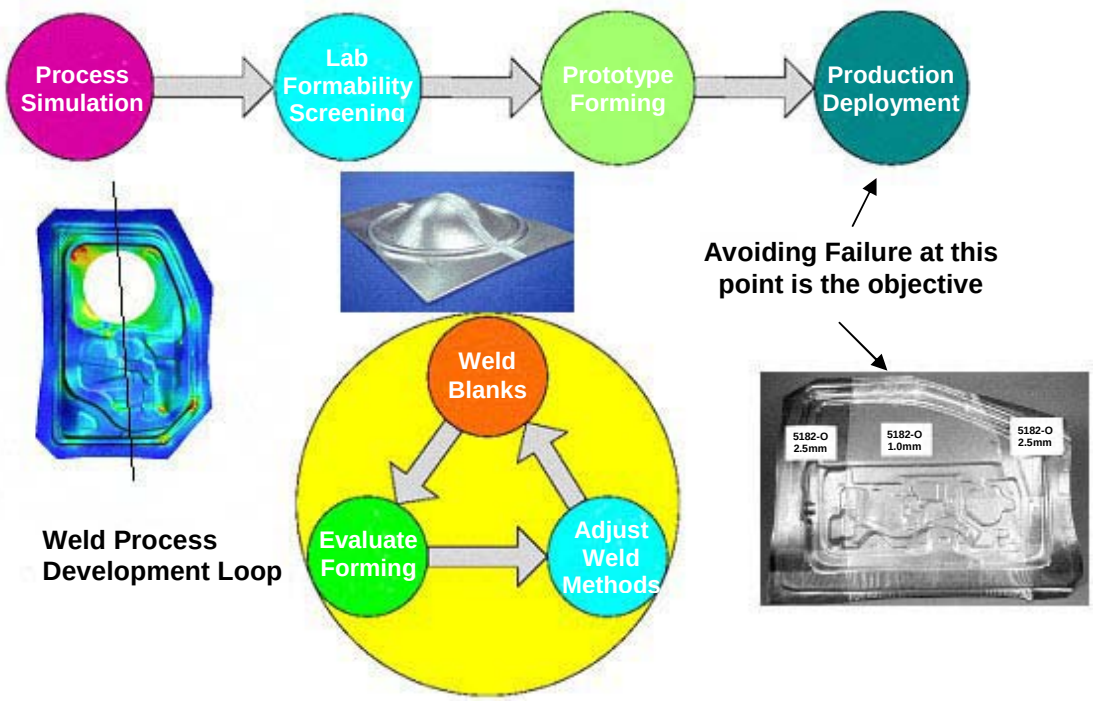

Figure 2. A schematic of the typical manufacturing process development.

fusion welds suffer from irregular geometries and elevated levels of surface roughness compared to the parent materials, which aspects also influence formability and component performance.

This project will focus on developing a generalized numerical method to predict material forming limits in weld materials and verifying deformation and forming-limit predictions. The approach will rely on developing standardized test methods for weld-material populations to establish a statistical description of material imperfection and mechanical properties in their weld region, and developing statistically-based, forming-limit diagrams or continuum damage models that predict material failure in the weld region.

The project will include numerical-model development, validation, and supporting experiments. A number of candidate weld methods will be examined in combination with selected Al alloys and AHSSs. The project materials will include 5000 series and 6000 series Al alloys and relevant high-strength steel alloys including high-strength low-alloy (HSLA), transformation-induced plasticity (TRIP) and dual-phase (DP) steels. The selection of sheet materials and welding methods will be coordinated with the participating OEMs and will be representative of high-volume, commercially-viable materials and processing technologies.

The deliverables will include a standard procedure for weld-material evaluation coupled with a numerical approach for establishing weld-region forming limits. The results will also allow evaluation and development of candidate weld processes and the interaction between materials and weld parameters. The overall objective is to develop test methods and experimental results to enable widespread deployment of weight-optimized TWB and tube hydroforming and to avoid weld failures during production. Figure 2 is a schematic of the typical manufacturing process development.

Experimental Characterization

This year, an increased focus on biaxial experiments occurred. Currently, the experimental characterization has focused on incorporating biaxial limited-dome-height (LDH) tests to FSW AA5182-O to AA5182-O alloys. Biaxial testing continued for the FSW AA5182-O to AA6111-T4 alloys and DP 600 laser-welded alloys. The

following details progress to date with greater emphasis on the 5182 welded alloy population. In the uniaxial experiments of 5182 FSW specimens, twenty-nine of the thirty longitudinal specimens failed in the thin sheet-grip region and all thirty transverse specimens also failed in the thin sheet-grip region. The TWB thickness combination for this population is 2 mm to 1 mm. Figure 3 illustrates the failure observed in both a longitudinal and a transverse specimen.

Miniature tensile tests performed on specimens removed from the weld and weld region indicated the weld material to be just as ductile and strong as the parent sheet. Figure 4 compares the stress-strain response observed in the parent sheet and weld material. Minimal mechanical property gradients across the weld and weld region were observed. This led to implementing a new test approach involving biaxial LDH tests to further characterize the 5182 FSW TWBs.

Biaxial LDH tests were performed on the 5182 welded alloys. Both full domes, 4-inch-wide domes, and 1.5-inch-wide domes were tested, with a minimum of five specimens tested for each condition. Smaller width domes were implemented to obtain uniaxial strain data since the smaller the width of the dome, the closer the behavior is to uniaxial. Full-dome tests were also conducted on the parent sheet material for the TWB combination. Digital-imaging correlation (DIC) was used to evaluate the specimens.

For the 5182 welded specimens, all full-dome biaxial tests failed in the thin sheet (Fig. 5). Testing then continued with the 4-inch-wide specimens; however, failures in the lock bead region of the thin sheet were observed when the same test conditions as in the full-dome-height tests were used. Figure 6 illustrates the failure observed. Failure in the lock bead is typically indicative of too large of a clamp load. When the clamp load was reduced, failures in the lock bead still occurred regardless of the pressure used even when excessive draw took place. An acceptable clamp load was ultimately found and much effort and care was put forth in specimen preparation and shimming of the specimen to reduce excessive failures in the lock bead.

Fourteen 4-inch-width specimens were tested at the same test conditions and six of the fourteen specimens failed in the weld transverse to the weld. Failure in the lock bead prevented the other specimens from reaching full height. Figure 7 illustrates the DIC strain data for a 4-inch width specimen.

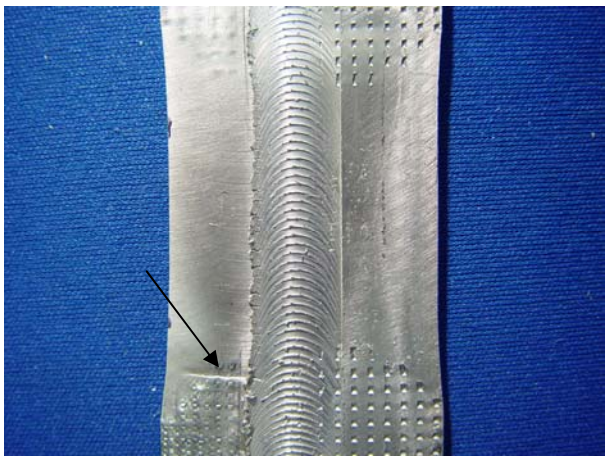

(a)

(b)

Figure 3. An illustration of the failure observed in the grip region of the 5182 welded alloy uniaxial speicmens. Image (a) is a longitudinal specimen and (b) is a cross-section of a transverse specimen.

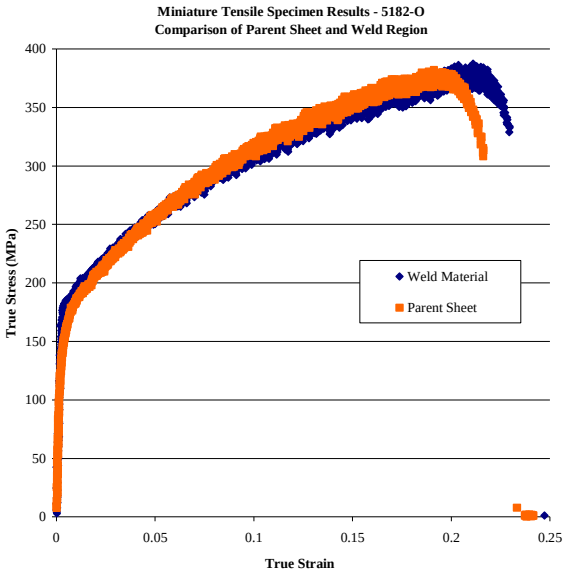

Figure 4. The stress-strain curves of the parent material and weld material of the 5182 TWB.

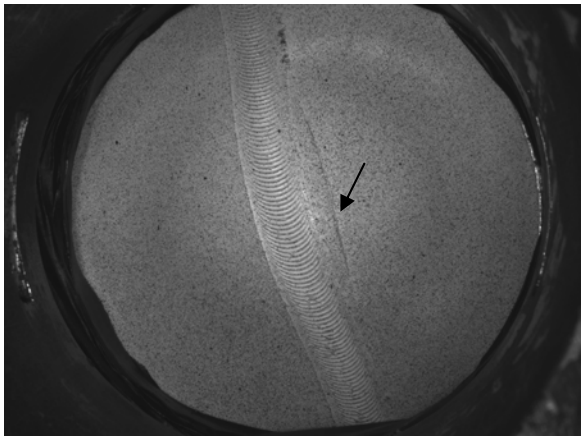

Figure 5. Photo representative of failure observed in the thin sheet of full-dome LDH tests of the 5182 TWB welded alloy.

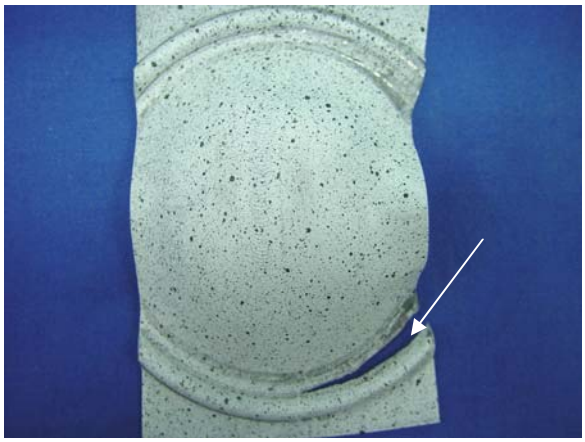

Figure 6. Photo representative of failures observed in the lock bead region of 4-inch and 1.5-inch LDH specimens.

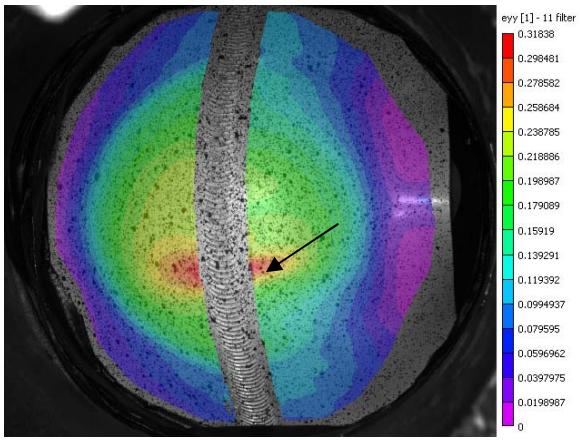

Figure 7. An illustration of the DIC strain data just prior to fracture on a 4-inch-width 5182 welded dome-eight specimen. Fracture occurred in the red region.

LDH tests of the 1.5- inch-width FSW 5812 specimens were not successful. All specimens tested failed in the lock-bead region of the thin sheet. Failure still occurred in the lock-bead region when a low clamp load was used that allowed excessive draw-in. When a monolithic, 1-mm-thick, 1.5-inch-width 5182 specimen was tested, failure was still observed in the lock-bead region. Modifications to the lock-bead radius may be needed to prohibit failure in the lock-bead region.

Due to the high quality of the weld, further analysis of the strain data is needed to determine how the biaxial results compare to the monolithic 5182 FLD. This will help determine whether further biaxial testing is viable.

Marciniak-Kuczynski (M-K) Method to Predict Formability

Previously, FLDs for the DP 600 and 5182-6111 TWBs were generated using a M-K method approach. The M-K model can track the development of plastic strains in the monolithic sheet and the weld materials under applied external loading. The model also tracks the evolution of imperfections and predicts localization and failure of the specimens. Theoretical FLDs are generated based on uniaxial tensile results and statistical probability. The level of imperfection, *f*, that must exist in the specimens in order to describe the formability for each of the thirty longitudinal specimens, is determined. A Weibull probability distribution is then applied to describe the longitudinal specimen imperfections and the predicted FLD for the TWBs is generated.

Previously, the 5182-6111 full-dome biaxial test experiments were compared to the theoretical FLD generated. Discrepancies of the model and biaxial experiments were observed, so all test results were combined in a FLD where the strain longitudinal to the weld and the strain transverse to the weld were plotted. The FLD of the parent sheet material (from literature) was also plotted. Figure 8 shows that there is a region in the FLD where the weld will always fail and a region where the sheet will fail. In between is a “gray area” where either the weld or HAZ of the thin-sheet 6111 material will dictate the failure.

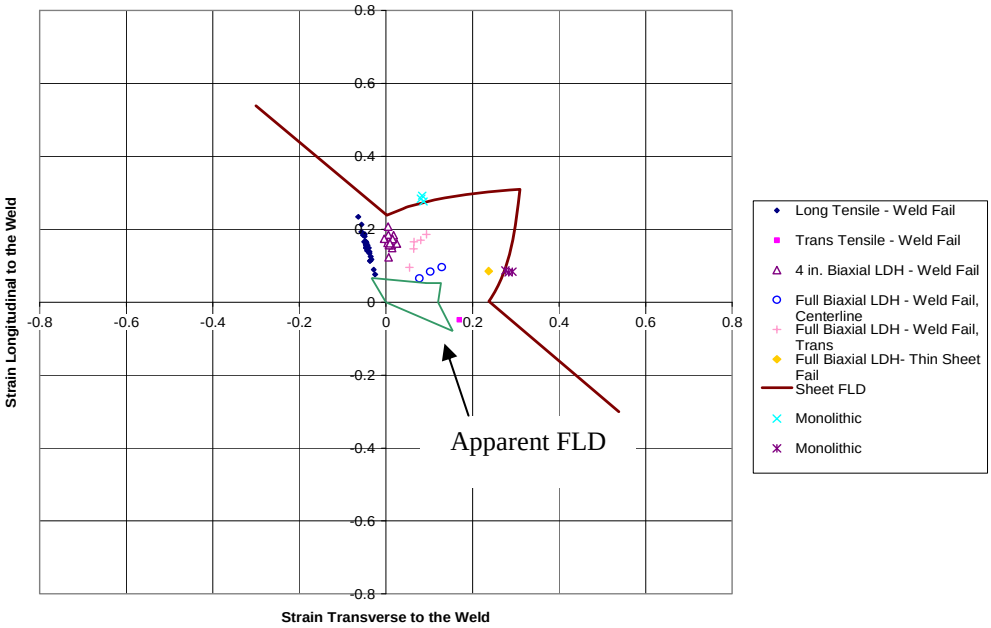

Figure 8. 5182-6111 friction-stir-welded materials combined test results demonstrating apparent FLD for the welded alloy population. The FLD for 6111 monolithic sheet is also shown.

Additional LDH tests were completed to further investigate how the FLDs would be suppressed in these "gray areas." Nine full-dome-width specimen tests and fifteen 4-inch-width specimen tests were completed. Three different failure modes were observed among the full-width specimens and all 4-inch-width specimens failed in the weld, transverse to the weld. Figure 8 demonstrates where the apparent FLD would be for this population. Further modification to the forming-limit prediction is still needed.

Conclusions

From this investigation, the following conclusions were derived:

- Due to the high quality of the weld, obtaining failures in the 5182 FSW alloys through biaxial testing proved to be difficult.
- Further analysis of the FSW 5182 strain data is needed to determine how the biaxial test results compare to the monolithic 5182 FLD to determine the viability of additional biaxial testing.
- Further investigation of a combined forming limit prediction of DP 600 and AA5182-6111 welded alloys is needed where the combined FLD is quantified using the statistical approach.

Presentations

1. *"Characterization and Formability of 5182-6111 TWBs"* presented at Materials Science & Technology 2007 Conference and Exhibition, Detroit, MI, September 17, 2007.
2. "*Forming Limits of Friction Stir Welded 5182-6111 TWBs*" presented at TMS 2007 Annual Meeting, Orlando, FL, and March 1, 2007.
3. *"Determining Aluminum Alloy Strain Localization under Biaxial Loading Using In-Situ Optical Strain Imaging"* presented at TMS 2007 Annual Meeting, Orlando, FL, March 1, 2007.
4. *"Forming Limits of Weld Material in Aluminum Alloys and High-Strength Steels"* presented to Industrial Team Advisory Committee, Detroit, MI, December 2006
5. *"Forming Limits of Weld Material in Aluminum Alloys and High-Strength Steels"* presented at USAMP AMD Offsite Annual Review Meeting, Detroit, MI, October 2006.

B. Impact Modeling and Characterization of Spot Welds

Principal Investigator: Zhili Feng
Oak Ridge National Laboratory (ORNL)
1 Bethel Valley Road, Oak Ridge, TN 37831
(865) 576-3797; fax: (865) 574-4928; e-mail: fengz@ornl.gov

Principal Investigator: Srjdan Simunovic
ORNL
1 Bethel Valley Road, Oak Ridge, TN 37831
(865) 241-3863; fax: (865) 574-7463; e-mail: simunovics@ornl.gov

Principal Investigator: Bill Chao
University of South Carolina
Columbus, SC 29208
(803) 777-5869; fax: (803) 777-0106; e-mail: chao@sc.edu

Technology Area Development Manager: Joseph A. Carpenter
(202) 586-1022; fax: (202) 586-1600; e-mail: joseph.carpenter@ee.doe.gov

Expert Technical Monitor: Philip S. Sklad
(865) 574-5069; fax: (865) 574-6098; e-mail: skladps@ornl.gov

---

Contractor: ORNL
Contract No.: DE-AC05-00OR22725

Objective

- Develop a new, robust Spot-Weld Element (SWE) for modeling various modes of spot-weld failure as a function of impact, welding conditions and materials while maintaining the current computational efficiency and ease-to-use.
- Develop the implementation procedure to incorporate SWE in crash-simulation finite-element analysis (FEA) codes used by the automotive crash modelers.
- Generate a companion experimental database on the performance of advanced high-strength steel (AHSS) spot-weld behavior under various loading conditions and deformation rates to support and validate the modeling approach.

Approach

- A new SWE and associated constitutive models.
- Modeling and characterization of weld microstructure and property.
- Deformation and failure-behavior testing under different dynamic-loading conditions.

Accomplishments

- Completed welding and welding-coupon preparation for dynamic testing.
- Completed static testing and dynamic testing.
- Initial correlation between failure load, failure mode and weld conditions under both static- and impact-loading conditions.
- Completed weld-quality assessment and microstructure characterization.
- Initial weld-element analytical formulation.

Future Direction

- Complete welding-process simulation of spot welds to provide detailed weld-property and attribute information for SWE development.
- Complete weld-failure criterion development.
- Complete development of SWE to demonstrate its basic characteristics meeting the intended modeling requirements.
- Deliver initial version of the SWE and its implementation procedure.

Introduction

A primary premise that drives increased use of AHSS in auto body structures is the drastic improvement in crash performance while reducing the weight. Resistance spot welding (RSW) is, by far, the most common joining process used in automotive manufacturing. Typically, there are thousands of spot welds in a vehicle. Because the separation of spot welds can affect the crash response of a welded structural component, the static and dynamic behaviors of the spot welds have been critically important considerations in vehicle design and manufacturing.

RSW of AHSS presents unique technical challenges for automotive structure applications. Due to their high carbon and alloying-element contents, AHSSs are considerably more sensitive to the thermal cycle of welding than the conventional steels used in auto body structures. The higher-grade AHSSs (e.g., dual-phase (DP) 800/1000, transformation-induced plasticity (TRIP), boron) are more difficult to weld and more susceptible to forming brittle microstructures and solidification-induced defects in the weld region. In addition, heat- affected zone (HAZ) softening can occur. Therefore, RSW of AHSS can exhibit very different structural performance characteristics than of conventional steels. For example, AHSS spot welds can fail under different failure modes (button pullout, interfacial, or mixed). In addition, impact experiments on joints and structural components (top-hat, double-hat sections) have shown that RSWs have different response under static and dynamic loads. The spot-welded structural performance among different AHSS can be drastically different and highly dependent on the grades and types of AHSS. Furthermore, there can be considerable variations in microstructure and properties in the weld region for a given type and grade of AHSS made by different steel producers due to the differences in steel chemistry and processing routes employed.

In recent years, computer-aided engineering (CAE)-based simulation of dynamic-impact behavior of auto body structure during crash has become an indispensable tool that enables rapid and cost-effective design and engineering of crash-resistance auto-body structures. Currently, the behavior of spot welds in finite-element modeling (FEM) impact simulations is usually modeled with a kinematics representation of the joint and the associated constitutive model describing the material-related response of the joint. Currently, the kinematics of the joint are treated as a point connection by means of flexible or rigid (i.e., constrained) links. The sophistication of these beam-link models is limited and can practically involve only force-based laws. One of the principal problems with beam-based kinematics models is that the stress and strain distributions in the weld area are not accurately represented. On the other hand, the maximum shear stress in the weld nugget could be the primary stress component causing the interfacial failure of RSW. For RSW in *conventional* steel structures, the dominant failure mode is the button pull-out and the inadequate calculation of the shear stress may not be a major concern in impact simulation of vehicles. For AHSS RSW, accurate determination of the shear stress may be critical because of the reported interfacial failure or mixed interfacial plus pull-out failure mode. In addition, the multiple failure modes and the changes in failure modes under different loading conditions require development of more versatile failure criteria based on the fracture- and damage-mechanics principles than the resultant force-based ones. From the structural stiffness perspective, the bar-and-beam models typically yield acceptable accuracy under tension, out-of-plane torsion and bending loads. However, the stiffness models are highly inaccurate for in-plane torsion and shear.

This program aims at developing a novel and robust spot-weld modeling approach supported by

experimental data that can be implemented in crash-simulation FEA codes used by the automotive crash modelers. The research tasks include: (1) developing a new, robust, spot-weld finite-element formulation and implementation procedure for modeling various modes of spot-weld failure as a function of impact, welding conditions and materials while maintaining the current computational efficiency; (2) performing coupon-level, dynamic testing to generate the experiment database of spot-weld performance under different loading modes and strain rates during impact; (3) developing failure criterion which can adequately deal with the failure mode changes usually encountered during dynamic loading of a spot weld; and (4) validation of the new crash-modeling approach by component-level crash testing.
This report covers the progress for the first 10 months of the program (December 2006 to September 2007).

Material Selection and Fabrication of Welds

Two steels, DP 780 and draw-quality special-killed (DQSK), were selected by the A/SP Strain Rate Characterization Project Team (see 5.G) for initial development in this project. A third steel, either Boron or DP 980, was considered in the later part of the project. The DP 780 steel had a nominal thickness of 1.15 mm. The nominal thickness of DQSK mild steel was 1.0 mm.

The selection of welding conditions considered the effect of weld-nugget size on failure mode during testing. Three target weld nugget sizes were chosen as the weld matrix for model development:

- Minimum nugget size per industry specification (provided by A/SP Joining Technologies Team): $4\sqrt{t}$ (where t = sheet thickness).
- Maximum nugget size attainable without expulsion: $5.5\sqrt{t}$.
- Medium nugget size = (min+max)/2.

The welding conditions were adjusted to produce the different sized welds.

Table ***1*** summarizes the welds and the associated welding conditions. The weld-nugget size (as determined by peel test) ranged from 4 to 6 mm.

Table 1. Summary of welding conditions and weld nugget sizes.

Weld Schedule Data									
Test	Material	Gauge	Coating	Specified Weld Size	Weld Size Range	Electrode Cap	Weld Force	Weld Current*	Weld Time
3806r1	DP780	1.15 mm	Galv'nel	4.3	4.1 – 4.5	A1 - 4.2	500	6.6	8
3806r2	DP780	1.15 mm	Galv'nel	5.1	4.9 – 5.3	A2 - 5.0	650	6.7	12
3806r3	DP780	1.15 mm	Galv'nel	5.9	5.7 – 6.1	A3 - 5.8	750	8.0	16
3806r4	Mild	1.00 mm	HDG	4.0	3.8 – 4.2	A4 - 3.9	400	7.7	8
3806r5	Mild	1.00 mm	HDG	4.8	4.6 – 5.0	A5 - 4.7	400	8.4	11
3806r6	Mild	1.00 mm	HDG	5.5	5.3 – 5.7	A6 - 5.4	550	9.7	15

Microstructure Characterization

Figure 1 shows the appearance of spot welds made under different welding conditions. There are drastic differences in weld microstructure between DP 780 welds and DQSK (mild steel) welds. More detailed microstructure characterizations are under way.

It is **also** important to point out the solidification shrinkage void at the center of DP 780 welds made to the minimum nugget size. The solidification-shrinkage-induced void was observed on replicate weld samples. Such defects may have contributed to the interfacial failure during quasi-static and impact testing.

Figure 2 shows the microhardness distributions of DP 780 and DQSK spot welds. Due to symmetry, only the top half of the spot weld was measured. The overall microhardness distributions of different-sized welds of the same steel made with different welding conditions are similar, with slightly higher hardness for the smaller welds. However, DP 780 exhibits very different microhardness and strength distribution from the DQSK steel. These differences will need to be considered in the formulation of the SWE.

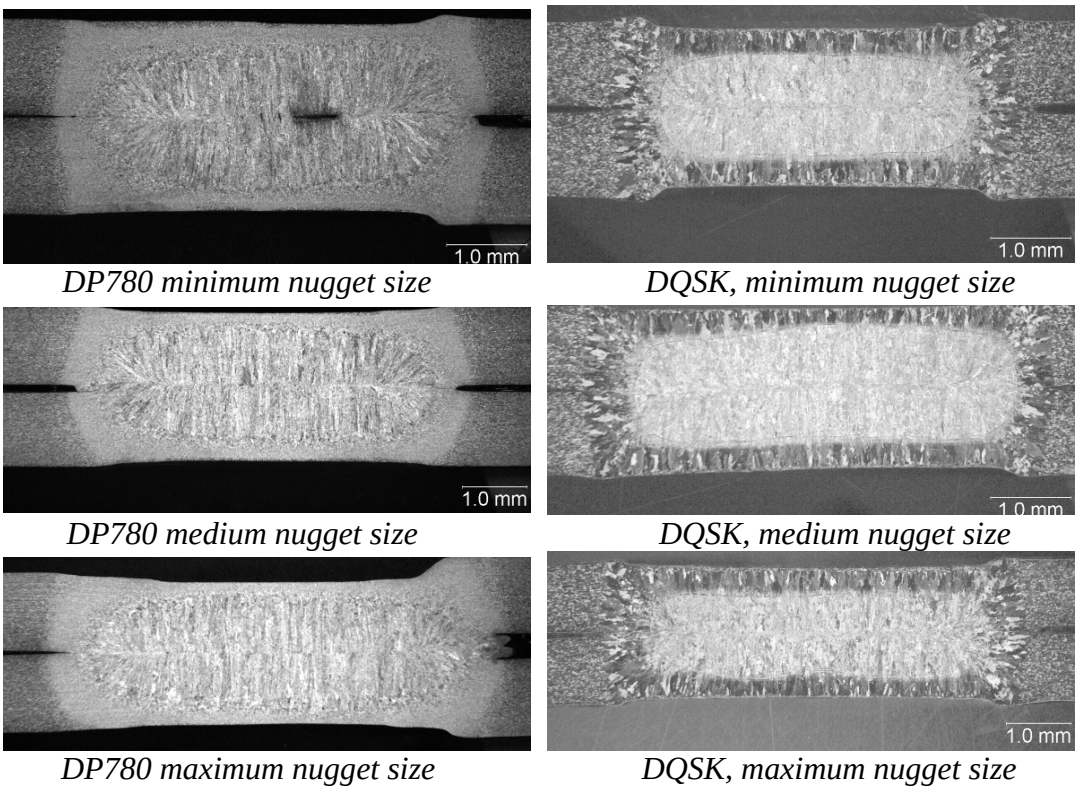

DP780 minimum nugget size *DQSK, minimum nugget size*

DP780 medium nugget size *DQSK, medium nugget size*

DP780 maximum nugget size *DQSK, maximum nugget size*

Figure 1. Weld nugget appearance of DP 780 and DQSK welds. Solidification void was observed in DP 780 welds.

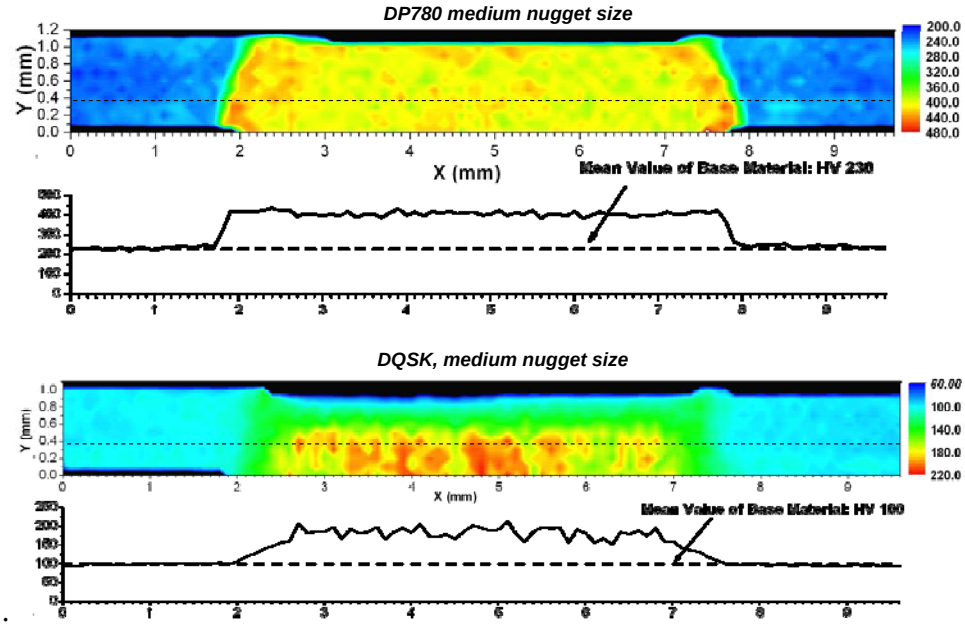

Figure 2. Microhardness mapping of spot welds. Only upper half of the spot weld is measured. The line plots show the hardness variations alone the dashed lines in the hardness mappings.

Impact and Static Test of Spot Welds

Both dynamic and static testing of the spot welds, in lap-shear, cross-tension, and mixed torsion/tension loading configurations, were performed. The test matrix included the followings:

- Two steels: DQSK, and DP 780.
- Three weld-nugget sizes: minimum specified, maximum without expulsion, and medium.
- Five loading modes: cross-tension, lap-shear, three combinations of torsion and tension at 0, 30 and 90 degrees.
- Four loading velocities: quasi-static, 2.6 m/s (5.8 mph), 3.6 m/s (8.1 mph), and 5.8 m/s (12.5 mph).

Standard lap-shear and cross-tension weld coupons were used in this study. The dimensions of the lap-shear coupon were 2-in. wide and 6-in. long, with the spot weld at the center of 2-in. overlap. The cross-tension coupons were also 2-in. wide and 6-in. long. A specially-designed coupon configuration was used for the mixed torsion and tension loading-mode testing. Figure 3 shows the mixed-load coupon design and the experimental set-up.

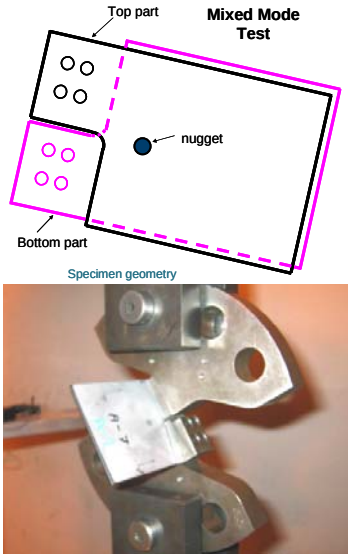

Figure 3. Mixed torsion/tension load weld coupon design and the experimental setup for mixed torsion/tension loading at 30 degrees.

Table 2 summarizes the failure modes observed during the lap-shear and cross-tension test for different loading rates and weld button sizes. For mild steel (DQSK), the failure mode is clearly related to the loading mode. All interfacial failure occurred under shear loading mode. For DP 780, interfacial failure is also associated to the shear loading, except for the minimum button-size case where a solidification-shrinkage void was observed. The weld size also has a pronounced effect; interfacial failure occurred when the weld is at the minimum or medium button size.

Table 2. Failure modes of spot welds in lap-shear and cross-section tests.

Material	Weld Button Size (mm)	Load Mode	Loading speed (mph)	Failure mode
DP780	4.3	CT	Static	Interfacial
DP780	4.3	CT	8.1	Interfacial
DP780	4.3	CT	12.5	Interfacial
DP780	5.1	CT	Static	Pullout
DP780	5.1	CT	5.8	Pullout
DP780	5.1	CT	8.1	Pullout
DP780	5.1	CT	12.5	Pullout
DP780	5.9	CT	Static	Pullout
DP780	5.9	CT	8.1	Pullout
DP780	5.9	CT	12.5	Pullout
DP780	4.3	LS	Static	Interfacial/Pullout
DP780	4.3	LS	8.1	Pullout
DP780	4.3	LS	12.5	Interfacial/Pullout
DP780	5.1	LS	Static	Pullout
DP780	5.1	LS	8.1	Pullout
DP780	5.1	LS	12.5	Interfacial/Pullout
DP780	5.9	LS	Static	Pullout
DP780	5.9	LS	8.1	Pullout
DP780	5.9	LS	12.5	Pullout
Material	**Weld Button Size (mm)**	**Load Mode**	**Loading speed (mph)**	**Failure mode**
DQSK	4	CT	Static	Pullout
DQSK	4	CT	5.8	Pullout
DQSK	4	CT	12.5	Pullout
DQSK	4.8	CT	Static	Pullout
DQSK	4.8	CT	8.1	Pullout
DQSK	4.8	CT	12.5	Pullout
DQSK	5.5	CT	Static	Pullout
DQSK	5.5	CT	5.8	Pullout
DQSK	5.5	CT	8.1	Pullout
DQSK	5.5	CT	12.5	Pullout
DQSK	4	LS	Static	Pullout
DQSK	4	LS	8.1	Interfacial
DQSK	4	LS	12.5	Interfacial
DQSK	4.8	LS	Static	Pullout
DQSK	4.8	LS	8.1	Interfacial/Pullout
DQSK	4.8	LS	12.5	Interfacial/Pullout
DQSK	5.5	LS	Static	Pullout
DQSK	5.5	LS	8.1	Pullout
DQSK	5.5	LS	12.5	Pullout

No inter facial failure was observed at the maximum weld size produced in this study. Increases in loading rate tend to promote the interfacial failure for lap-shear loading condition.

The effect of weld-button size on the failure load of spot welds is provided in Figure 4. The data

presented include all the loading rates under lap-shear and cross-tension. Clearly, failure strength is proportional to the weld size. DP 780 has much higher failure strength than DQSK. The effect of the loading rate (impact velocity) is shown in Figure 5. For comparison between different steel grades, the failure load is normalized to that under the static-loading case. The effect of loading rate (strain-rate sensitivity) was clearly observed. Overall, the failure strength generally increases as the strain rate increases. However, the degree of strain rate sensitivity is rather complicated – it appeared to be strongly related to the steel grade and the loading mode. Further data analysis is under way to quantify the effect of strain-rate sensitivity.

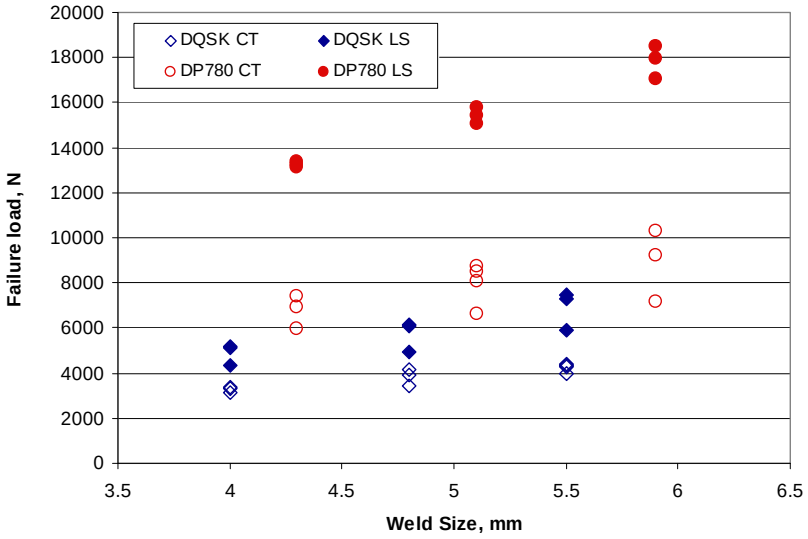

Figure 4. Effect of weld size on the failure load of spot welds.

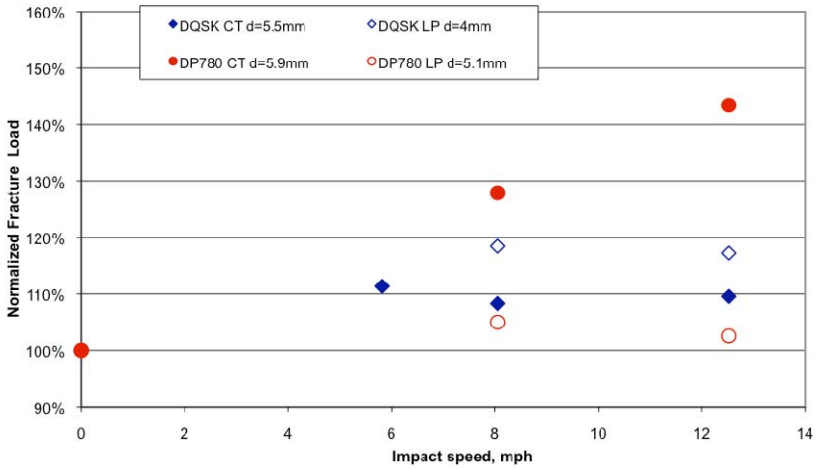

Figure 5. Percentage change of failure load as function of loading rate (impact speed).

Development of Spot Weld Element

A new FEM element formulation, the SWE, based on constraints between thick shell element for modeling of sheets and solid elements for model ing of spot-weld zone, has been developed. Shell degree of freedoms (DoF) are coupled with solid Element DoF using constraints that are connecting shell-element displacements and rotations of its mid-surface with displacements in the solid element. The objective is to provide a better model

for transfer of loads through the spot weld. The better description of the forces and deformations in the spot weld will allow for utilization of more accurate failure criteria based on stresses in the HAZ and the weld nugget.

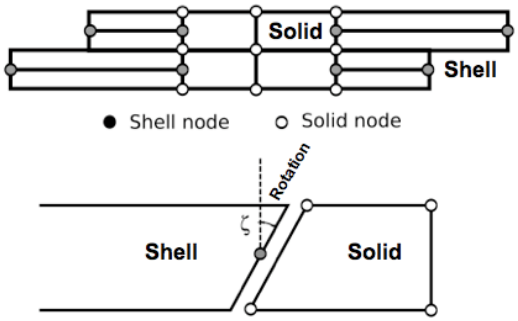

Figure 6. Spot-weld zone representation using shell and solid elements.

Two formulations are being explored. The first formulation depicted in Figure 6 is based on coupling rotational and displacement degrees of freedom between the shell (sheet metal) and the solid (spot-weld nugget). The second formulation (Figure 7) uses thick shell elements in the HAZ to better couple through-thickness stresses.

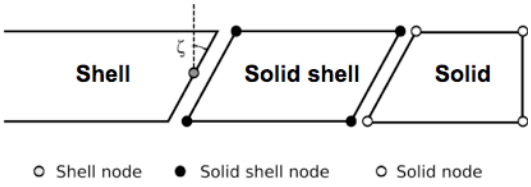

Figure 7. Spot-weld model using tick shells for HAZ.

The analytical expressions defining the mapping of DoF between the elements have been developed. Current shell-element discretization for crash-model sizes are often of the same order as weld diameter and it is, therefore, feasible to introduce a new modeling entity of the RSW dimensions.

The solid elements use eight nodes which provide sufficient flexibility for representation of the stress and strain fields within the RSW zone. Stress distribution in solid elements and element geometry can be used to introduce fracture toughness of the interfacial region in the failure criteria. Mesh refinement of the weld zone is straightforward and non-conformal meshes can also be explored. It is expected that the constitutive models to be used in a SWE will be based on strain-rate sensitive, elasto-plastic fracture- and damage-mechanics models. The actual material models will need to be first evaluated in the context of RSW as such efforts have not been reported in the open literature. The coupling of the constitutive model to the SWE will require more sophisticated element failure and removal strategy than is currently available in commercial software.

Initial simulations using the above formulations were performed on lap-shear, cross-tension and mixed-mode specimens (Figure 8 to Figure 10, respectively).

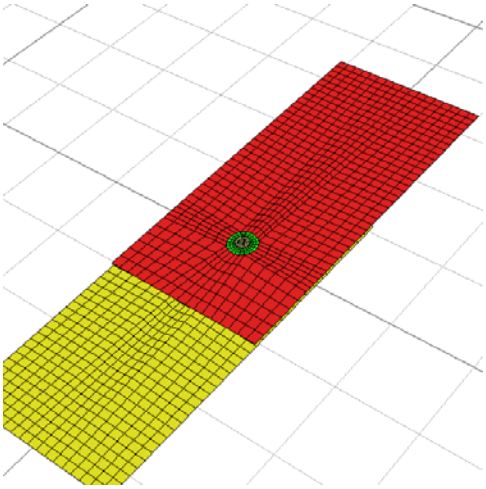

Figure 8. Lap-shear spot-weld model.

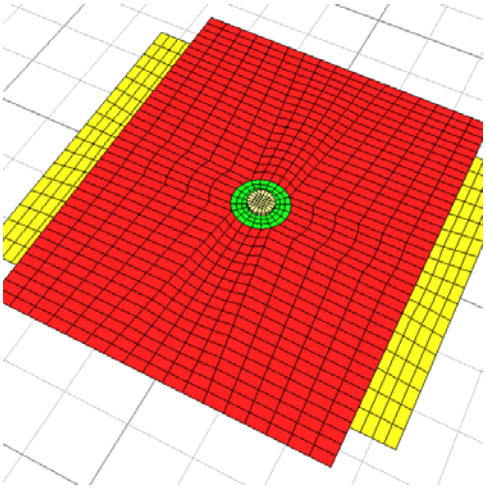

Figure 9. Cross-tension spot-weld model.

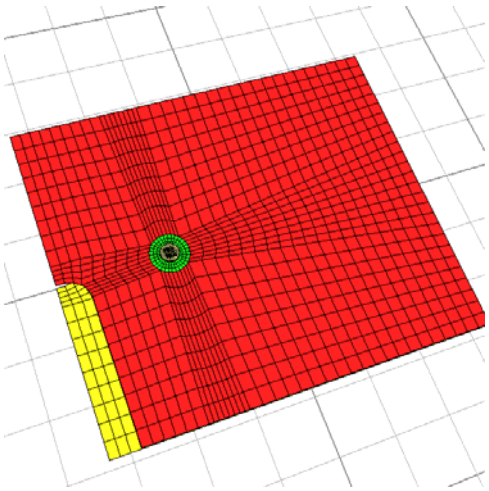

Figure 10. Mixed-mode spot-weld model.

Models are using very fine finite-element meshes in order to remove artifacts due to mesh sensitivity, and the final models will employ much coarser discretization. Simulation results are compared with the experiments to develop failure criteria for the spot welds. The deformations prior to the spot-weld failure are in good agreement with the experiments. Various failure criteria are currently being explored for inclusion into the overall spot-weld model.

Plan for FY2008

- Complete welding-process simulation of spot welds to provide detailed weld- property and attribute information for SWE development.
- Complete weld-failure criterion development.
- Complete development of SWE to demonstrate its basic characteristics meeting the intended modeling requirements.

C. Friction-Stir Spot Welding of Advanced High-Strength Steels

Principal Investigator: Michael L. Santella
Oak Ridge National Laboratory (ORNL)
1 Bethel Valley Road, Oak Ridge, TN 37831-6096
(865) 574-4805; fax: (865) 574-4928; e-mail: santellaml@ornl.gov

Principal Investigator: Glenn J. Grant
Pacific Northwest National Laboratory (PNNL)
902 Battelle Boulevard, P.O. Box 999, Richland, WA 99352
(509) 375-6890; fax: (509) 376-6034; e-mail: Glenn.Grant@pnl.gov

Principal Investigator: Yuri Hovanski
PNNL
902 Battelle Boulevard, P.O. Box 999, Richland, WA 99352
(509) 375-3940; fax (509) 376-6034; e-mail: Yuri.Hovanski@pnl.gov

Technology Area Development Manager: Joseph A. Carpenter
(202) 586-1022; fax: (202) 586-1600; e-mail: joseph.carpenter@ee.doe.gov

Expert Technical Monitor: Philip S. Sklad
(865) 574-5069; fax: (865) 576-4963; e-mail: skladps@ornl.gov

Expert Technical Monitor: Mark Smith
(509) 375-4478; fax: (509) 375-4448; e-mail: mark.smith@pnl.gov

---

Contractor: ORNL and PNNL
Contract Nos.: DE-AC05-00OR22725 and DE-AC06-76RLO1830, respectively

---

Objective

- The primary objective of this project is to develop friction-stir spot welding (FSSW) as a superior method to join advanced high strength steels (AHSS).
- Phase 1 activities will address the critical questions of whether there are tool materials available that have potential for reasonable life and whether FSSWs made in high-strength steels are feasible and can develop similar or better mechanical performance than welds made by conventional processes like resistance spot welding (RSW).
- Phase 2 activities will seek to increase joint strength through a more thorough investigation into weld-process parameters and tool design. This will be accomplished both explicitly using new tools and refined operating parameters and by means of modeling both the process and fundamental conditions applicable to FSSW.

Approach

- The project is in collaboration between ORNL and PNNL, and includes an advisory committee with representatives from Chrysler, Ford, General Motors (GM), two automotive-steel suppliers, and a friction-stir-welding tool supplier.
- Lap joints are made and used to correlate tensile shear strength with processing parameters and microstructures.

- Tool durability is evaluated by measuring tool wear after and during test programs and by characterizing the tool strength with changing welding conditions.
- Process modeling will be developed to help define optimum processing conditions and tool geometries.

Accomplishments

- Test programs fabricating spot welds in dual phase (DP) 780 and hot-stamped boron steel (HSBS) were initiated; a wide range of weld parameters were investigated.
- Fabricated coupons were subjected to metallographic examination, hardness testing, and lap-shear tests.
- Metallurgically-bonded areas in the weld nuggets were measured, characterized, and found to be smaller than expected; therefore, tools were redesigned to more effectively bond AHSS via FSSW.
- Initially, two tool materials (tungsten 25% rhenium [W25Re] and polycrystalline cubic boron nitride [PCBN]) and three tool geometries were investigated.
- Trials showed that tool wear in PCBN was low, but tool wear in W25Re was high.
- Mechanical testing of Phase 1 lap-shear coupons in DP 780 and HSBS indicate that, while overall strengths for certain weld parameters are in the range of acceptable values defined by the Draft American Welding Society (AWS) specification for RSW of steel, the specific strength of nearly any condition exceeds the minimum stress condition.
- Mechanical testing of FSSWs joined via Phase 2 tools produced dramatic increases in lap-shear strength when compared to the results from FSSWs produced with Phase 1 tools.
- Testing with Phase 2 tools further established the significant relationships between tool design, process parameters and weld material.
- Numerous evaluations of Phase 2 tools were made in both HSBS and DP 780, producing lap-shear strengths greatly exceeding the AWS D8.1M RSW minimum standard.
- Two new tool materials, silicon nitride (Si_3N_4) and titanium diboride (TiB_2) were used to produce several tools that are currently being evaluated.

Future Direction

- Further develop a process model linking factors critical to industrial implementation including total spot cycle time, tool wear and weld performance with changes in process parameters, tool materials and tool design.
- Evaluate the effects of steel corrosion coatings (hot-dipped galvanized and galvaneal) on the FSSW lap-shear strength.
- Produce a statistical evaluation of FSSW strength in both lap-shear and cross-tension.
- Establish the framework of a design database for spot friction-welded structures.

Introduction

The technology for implementing FSSW of aluminum (Al) in automotive manufacturing environments exists. C-gun-type FSSW heads have been developed and adapted to robotic systems that are now commercially available for FSSW of Al alloys. This project addresses the questions of whether the FSSW process is viable for joining AHSS and whether FSSW has advantages over conventional processes like RSW. Preliminary work on FSSW of AHSS suggested that several features of the process (fine-grained microstructure in the nuggets of AHSS, potentially higher-strength joints and higher energy absorption in crash, low energy consumption and environmental emission during manufacturing) may give FSSW cost and energy-saving advantages over RSW. In addition, the process may be viable for high-strength,

lightweighting alloys that currently have joining problems using conventional techniques (DP 1000, martensitic steels such as HSBS, etc.).

Important questions remain about effective, economical application of FSSW to AHSS. Critical questions being addressed in this study include:

- Are tool materials available that have potential for reasonable life?
- Are joint strengths comparable or better than conventional processes?
- Are manufacturing issues appropriate (cycle time, tool wear, process robustness and sensitivity to production variation)?
- Do FSSW joints have any advantage for nondestructive evaluation (NDE), or for real-time process control over RSW?
- Are total life-cycle costs appropriate?
- Can the process be modeled and predictive tools developed to aid designers?

If the effectiveness of FSSW for joining AHSS is established, it could accelerate the insertion of these high-strength, lightweighting alloys into automotive body construction to help meet FreedomCAR goals.

Approach

The primary objective of this project is to characterize the responses of AHSSs to FSSW. The project is organized into two phases. Phase 1 activities addressed the critical questions of whether there are tool materials available that have potential for reasonable life and whether FSSWs made in high-strength steels could develop strengths comparable to those made by conventional processes like RSW. Phase 2 objectives focus on the factors crucial to industrial implementation of FSSW; therefore, the second phase of the project concentrates on evaluation of several specific targets including cycle time, tool durability, process robustness, and repeatability.

The Phase 1 results, combined with the initial work under Phase 2, highlight two important challenges: the development of robust tool materials and the development of weld parameters needed to achieve consistently-high joint strengths. Presently, PCBN is the most durable, effective material from which to make stir tools for welding of steels. PCBN is relatively expensive. It is also difficult to machine into the needed shapes and it is not widely available for purchase. These characteristics significantly complicate modifying tool designs, but such modification is a critical element of maximizing joint strengths. In addition, the intrinsic durability of PCBN is not well characterized. There is considerable interest in identifying and evaluating alternatives to PCBN, particularly any that would reduce tool costs and improve durability.

A second set of challenges, framed by prior work, relates to developing consistently-high joint strengths. Joint strengths are being obtained which compare favorably with minimum values specified in industry standards for spot welds, such as AWS D8.1M. However, the consistency of obtaining these strength levels must be improved. In addition, welding times must be minimized. These conditions can be met by increasing the bonded area of FSSWs. Clearly, both sets of issues, those related to tooling and those related to joint strength, are interrelated.

Besides addressing the issues discussed above, Phase 2 intends to encompass developing a more detailed process model which includes weld-performance prediction, evaluating joint microstructures and mechanical properties, assessing the potential for in-process NDE, and establishing the framework of a design database for spot friction-welded structures. The project is a 50/50 collaboration between ORNL and PNNL, and it includes an advisory committee with representatives from Chrysler, Ford, GM, Mittal Steel Corp., and Gestamp US Hardtech, Inc.

Materials and Experimental Details

Presently, two uncoated high-strength steels are being used for the FSSW studies: the DP 780 and a HSBS (sourced from a Swedish supplier, the parent of US Hardtech). The DP 780 is 1.5-mm-thick sheet; the thickness of the HSBS sheet is 1.4 mm.

The FSSW performed during Phase 1, as well as during the initial portion of Phase 2, were done

nearly exclusively with PCBN tools. However, during the Phase 2 program, several new tool materials are being evaluated including Si_3N_4, TiB_2 and a new W-based cermet alloy. These materials are currently under investigation as lower-cost alternatives for FSSW tool materials.

All spot welds were made in displacement-control mode by varying the parameters of tool plunge depth and tool-plunging rate. In addition to these control parameters, a number of other process variables are typically recorded for each weld, including weld time, spindle torque, normal force, and temperature, on the back side of the two-sheet stack-ups. This additional information is archived for future use and analysis.

Joint strength is being evaluated by tension testing lap joints to determine their shear-tension strengths. Strengths are being correlated with processing parameters and microstructures. Micro-hardness mapping is also being used to assess the characteristics and properties of the joints.

Results and Discussion

Previously-reported results confirmed that FSSW has the potential to produce joints that meet strength minimums specified by AWS D8.1 for RSWs. However, the initial results also showed that developing high joint strength was related to producing large bonded areas in the FSSWs. It was further deduced that obtaining large bonded areas depended directly on weld parameters, primarily plunge depth, for a particular tool tip length. The results also illuminated the need for carefully matching tool designs to the sheet thicknesses being welded.

Based on the results from the initial work, four new PCBN tools (BN97, BN98, BN99 and BN46) were designed with the intent of increasing the overall bonded area of the FSSWs. Pin lengths were shortened on the BN97, BN98, and BN99 tools to force their shoulders to engage deeper into the top sheet of two-sheet stack-ups. The pin geometries were also altered to enhance the stirring action of the tools. Additionally, one tool, BN46, was designed with a convex shoulder and short, threaded pin with the intent of stirring and bonding larger regions in shorter weld times. Photographs of these four tools are presented in Figure 1.

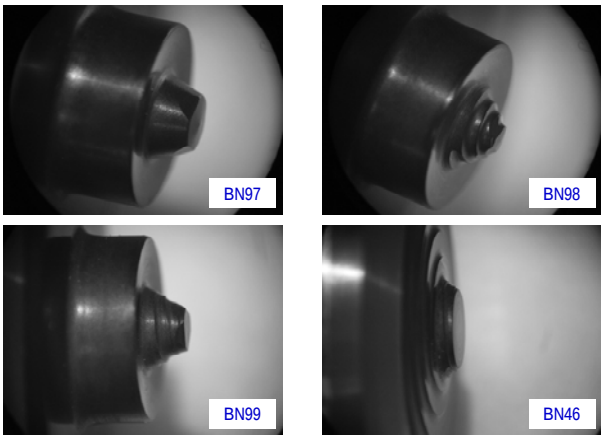

Figure 1. Initial Phase-2 Tools.

The effects of small modifications to tools design are illustrated by the shear-tension strength plots shown in Figure 2. The top plot is of the strength data obtained for DP 780 joints made with the BN77 tool from Phase 1 using plunge depths of 2.7-2.9 mm. The bottom plot shows the strengths measured for joints made with the same plunge depths using the BN99 tool. The solid line in both plots represents a minimum strength for RSWs in 1.5-mm-thick DP 780. Using the BN77 tool, only 2 of 21 specimens exceed the AWS D8.1 minimum. In contrast, 10 of 16 specimens exceeded this limit using the BN99 tool.

Further evaluation of Phase-2 tooling provided greater insight into the affect of tool geometry on weld performance. All four tools showed a marked increase in joint strength, in both DP 780 and HSBS, compared to their Phase-1 counterparts; however, specific performance varied dramatically based on weld material, surface preparation, and weld parameters. Figure 3 shows charts of joint strengths in both AHSS for a FSSW made at 800 rotations per minute (RPM) in 10-second duration. Such data demonstrate the effective differences of tool performance under similar operating conditions in various materials.

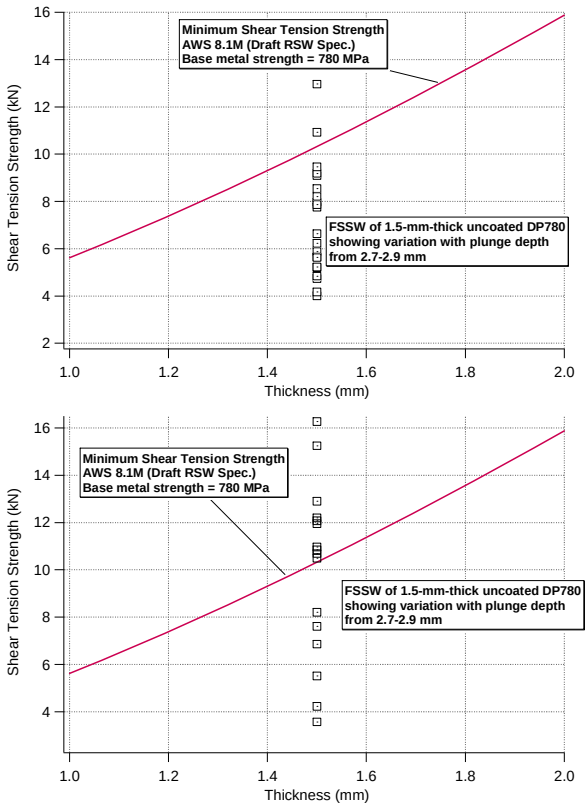

Figure 2. Shear-tension strengths for joints made to plunge depths of 2.7-2.9 mm with (top) BN77 tool (Phase 1), and (bottom) BN99 tool.

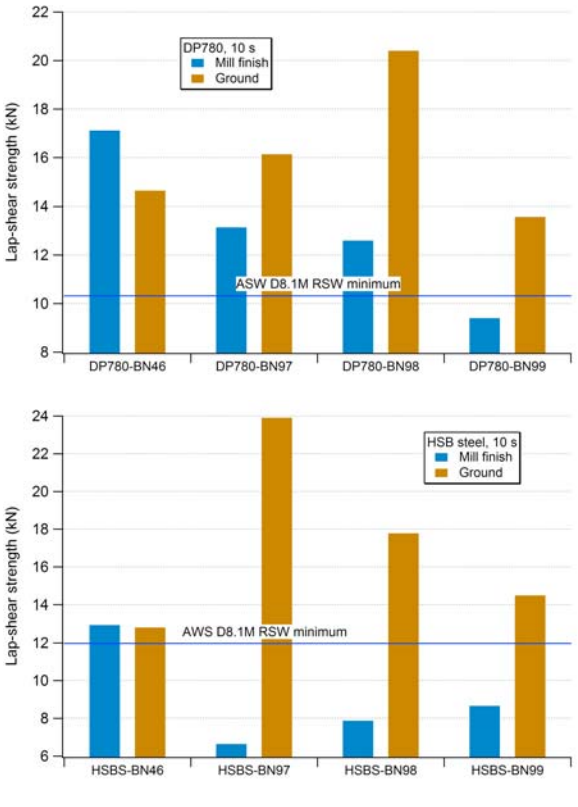

Figure 3. Shear-tension strengths for joints made to plunge a depth of 2.9 mm at 800 RPM in 10 seconds. FSSWs with all four Phase 2 tools in DP 780 (top) and HSBS (bottom).

As performance of the three pin tools (BN97, BN98 and BN99) greatly varied with surface preparation, all data presented in Figure 3 are displayed for joints made in both surface-ground and mill-finish surfaces. The BN46 showed less variability associated with surface preparation and achieved joint strengths above the AWS D 8.1 minimum standard for both DP 780 and HSBS.

An example of the associated microstructure formed using this less-conventional FSSW tool is illustrated in Figure 4. This optical micrograph shows a FSSW made in DP 780 with the BN46 tool. The overall effect of this tool design was to produce a wider, shallower pin cavity. For this particular weld, the plunge depth was actually less than the 1.5-mm thickness of the DP 780 sheets. The overall effect of this approach was to produce what appears to be a much larger bonded area between the two individual sheets than is typical of more conventionally-shaped tools like BN97, BN98, and BN99.

Figure 4. Optical micrograph of FSSW made in DP 790 using the BN46 stir tool.

A sense about the possible differences in properties between FSSWs and RSWs is illustrated in Figure 5. The top two images in this figure are optical micrographs showing a FSSW (upper image) and a RSW (lower image) made in DP 780. The bottom two images are representations of the joint made using data from micro-hardness mapping. Identical scaling was used in both the hardness images with the colors indicating the variations in micro-hardness across the welds. The hardness images confirm that both welds are harder than the DP 780 base metal. However, the weld nugget of the RSW is about

25% higher than that of the stir zone of the FSSW. Additionally, the heat-affected zone (HAZ) of the FSSW is much wider than that of the RSW. These characteristics of the FSSW will influence their overall mechanical behavior and will be addressed in continuing efforts.

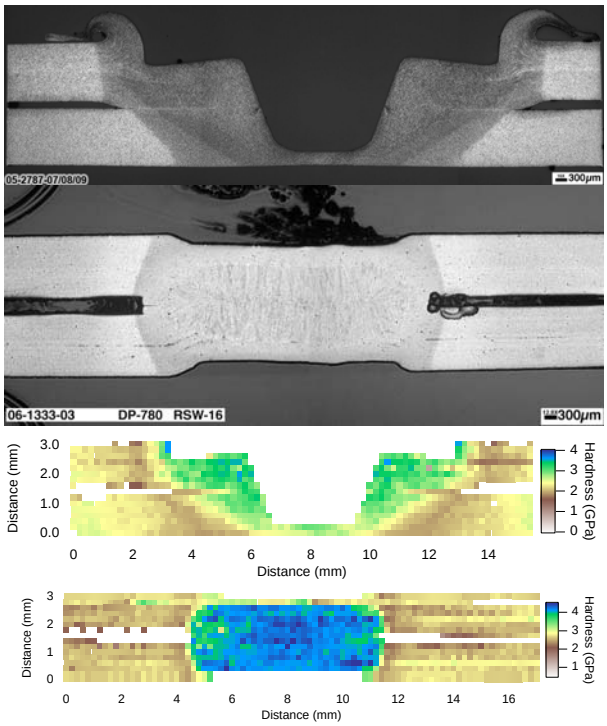

Figure 5. Top two images show optical micrographs of DP 780 FSSW (upper) and RSW (lower). The bottom two images are representations of each weld formed from micro-hardness test data.

Conclusions

During this reporting period, four new PCBN stir tools were designed and produced. Numerous testing conditions were found which produced spot welds that exceed industry-specified minimum strengths for 1.5-mm-thick DP 780 steel and 1.4-mm-thick HSBS.

One of the four new stir tools is a new approach in FSSW tool design. Examination of initial FSSWs made with this tool (BN46) on both AHSSs suggest that it is capable of producing larger bonded areas than those achieved with more conventional pin tool designs. This tool also showed less variability in joint strength with changes in surface preparation than the other Phase-2 tools.

Metallographic examinations showed that in DP 780 the weld-zone hardness of a RSW was about 25% higher than that of a FSSW. Both weld zones had higher hardness than the DP 780 base material. The HAZ of the FSSW was also significantly wider (> 3 mm) than that of the RSW (~ 2 mm). The implications of these differences will be addressed in the continuing testing program.

Finally, several new tool materials were selected for evaluation, including Si_3N_4, TiB_2 and a tungsten-based cermet that does not use the conventional cobalt binder. These tool materials are currently being evaluated and will continue to be investigated during the upcoming year.

Presentations/Publications/Patents

1. Y. Hovanski, M.L. Santella and G.J. Grant. Friction Stir Spot Welding of Hot-Stamped Boron Steel. Scripta Materialia, 57 (2007) 873-876.
2. Y. Hovanski, M.L. Santella and G.J. Grant. Friction stir spot welding of advanced high strength steels. Presentation at MS&T Sept. 2007.
3. Grant GJ, Y Hovanski, and M Santella. 2007. "Friction Stir Spot Welding of Advanced High Strength Steels for Automotive Applications." In: International Symposium on Friction-based Spot Welding Processes, eds. A.M da Silva, J.F.dos Santos, G. Amancio, International Institute of Welding, GKSS Forschungszentrum, Geesthacht, Germany, 2007, pp. 107-148.

D. Thermal-Drilling Application Development

Co-Principal Investigator: P. J. Blau
Oak Ridge National Laboratory (ORNL)
P.O. Box 2008, Oak Ridge, TN 37831-6063
(865) 574-5377; fax: (865) 574-6918; e-mail:blaupj@ornl.gov

Co-Principal Investigator D. M. Paxton
Pacific Northwest National Laboratory (PNNL)
P.O. Box 999/K2-03,Richland, WA 99352
(509) 375-2620; fax: (509) 375-2186; e-mail:dean.paxton@pnl.gov

Participants:
This project is being conducted as a partnership with the United States Automotive Materials Partnership (USAMP), Automotive Metals Division (AMD), with participation that includes the following representatives:

Bill Charron, Ford Motor Company
Larry Krawczak, Chrysler Corporation
Ron Strong, General Motors (GM) Corporation

Technology Development Area Manager: Joseph A. Carpenter
(202) 586-1022; fax: (202) 586-1600; e-mail: joseph.carpenter@ee.doe.gov

Expert Technical Monitor: Philip S. Sklad
(865) 574-5069; fax: (865) 574-6098; e-mail: skladps@ornl.gov

---

Contractor: ORNL and PNNL
Contract No.: DE-AC05-00OR22725 and DE-AC06-76RLO1830, respectively

---

Objectives

- Determine the feasibility of using thermal drilling (ThD) to form fastener holes in high-strength steels and light-weight alloys in the form of castings, hydroformed parts, and sheet stock.
- Determine suitable ThD parameters for selected alloys if they prove to be amenable to the process.
- Thermally drill and tap fastener holes, measure their dimensions, and conduct clamp-load tests to compare the properties of ThD holes to traditionally-produced fastener holes.
- Develop a better fundamental understanding of the ThD process.

Approach

- Alloys for ThD tests were selected and provided by the USAMP project team. ThD bits were purchased or provided as in-kind contributions from tool suppliers.
- ORNL conducted ThD and tapping experiments on the selected alloys, noting which performed best. Hole dimensions and microstructures were documented.
- Where possible, methods were developed to correct any observed hole defects. These included the use of pre-heating and pilot holes. Needs for future process development were documented.
- Maximum fastener clamp loads were measured at PNNL and related to ThD parameters.

Accomplishments

- Established the feasibility of ThD four high-strength steels and six non-ferrous alloys (Al and Mg-based).
- Developed a method of using pilot holes prior to ThD to avoid 'flower-petal' defects in Al alloys.
- Demonstrated that hydroformed high-strength-steel sections were highly suitable for ThD.
- Compiled a list of ThD process parameters for the selected alloys and included it in the final report.
- With one exception, demonstrated that steels were found to be generally more suitable for thermal drilling than the non-ferrous Al and Mg alloys. In fact, ThD and tapped holes in steel sheet thicker than 2.0 mm were so strong that the fastener broke rather than stripping the threads.
- Clamp-load testing was completed on all alloys that could be thermally drilled satisfactorily.
- A comprehensive final report was prepared, submitted to the USAMP team for review, and published.

Future Directions

- Contingent on new funding, optimize ThD on hydroformed steels to produce demonstration articles.
- Investigate new tool-bit designs and establish the feasibility of ThD multiple layers.
- Improve the ThD process to enable better quality results on non-ferrous alloys.

Introduction

The research on this project concluded in mid - fiscal year (FY) 2007 and the major findings will be presented in a final report currently under internal review. The concluding summary is repeated here.

Thermal drilling (ThD), also known as 'friction drilling,' is related to other joining and surface-conditioning processes like friction-stir welding and friction-stir processing that utilize frictional heat generated between a rotating tool and a metal part. In ThD, a conically-tipped tool (usually metal-bonded tungsten carbide) spins against the surface of the part to be drilled, generating heat and softening the surface. It penetrates and then perforates the workpiece, as shown in Figure 1. Softened material is extruded to form a bush on the exit side of the workpiece. A small boss may also be formed on the entrance side, under the shoulder portion of the tool. Another version of the tool has a cutter to remove the boss.

ThD is currently used in the manufacture of tubular hospital furniture and certain niche applications, but has not been adopted in the automotive industry where it has significant potential to enable more extensive use of lightweight, high-strength alloys.

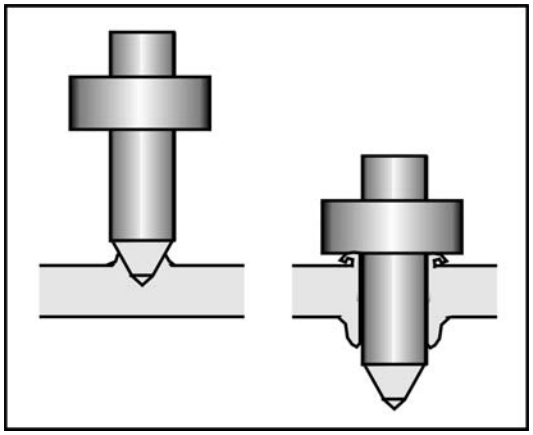

Figure 1. Schematic representation of ThD. The spinning tool penetrates the workpiece (left) to form a boss on the inlet side and a bush on the exit side (right).

Advantages of ThD include the following:

- Unlike traditional drilling, ThD creates no chips.
- ThD does not require drilling fluid that must be handled and disposed of.
- By forming an extruded bush, ThD thickens the effective tappable thickness of thin workpieces like sheet stock and thin-walled castings, so that weld nuts (with their added weight and assembly operations) may not be needed.
- ThD may enable designs that would be impossible due to the need to install nuts or get at the exit side of the hole.

- ThD could simplify manufacture of chassis components from lightweight materials.

The goal of this project was to demonstrate the feasibility of using ThD on selected ferrous and non-ferrous alloys of interest to the automotive industry and to acquire clamp-load data to measure the fastener holding capabilities of ThD and tapped alloys. These alloys are listed in Table 1. Thickness ranged from about 1.12 to 4.1 mm depending on the materials provided and their form.

Table 1. Materials provided for thermal drilling studies.

Alloy	Form
Al A380	Die casting
Al A319-T5	Die casting
Mg AZ91	Die casting
Mg AM60	Die casting
Mg AE44	Die casting
Mg AM50	Die casting
DP 600 HSS	Sheet
DP 780 HSS	Sheet
DP 780 HSS	Hydro-formed tube
HSLA50 HSS	Sheet
TRIP 800 HSS	Sheet

Technical Approach

The technical approach drew on the strengths of USAMP team members and national laboratories. It consisted of a drilling feasibility study at ORNL that established the ThD parameters that would produce acceptable holes (demonstrated, but not optimized) and clamp-load testing of fasteners in ThD and tapped holes at PNNL. ORNL also made measurements of hole dimensions for the range of drilling conditions that were investigated.

The ThD process variables included the following: (a) hole diameter (drill-bit diameter), (b) drill length, (c) spindle speed, (d) in-feed rate, (e) stock thickness, (f) use of drilling paste, (g) use of pre-heating or pilot holes, (h) use several types of bits, and (i) use of thread-cutting or thread-forming taps. Additional details of the task plan were provided in prior project reports and will be in the final report.

Results

A qualitative assessment of thermal drillability was made based largely on visual observations of the quality of the bushes created using bits for M6-sized holes. Table 2 summarizes these assessments. The designation codes were:

- **Poor** (***P***) – not suitable (distorted or torn bushes)
- **Marginal** (***M***) – might work but requires additional studies and process enhancements
- **Special Procedures** (***SP***) – satisfactory results are obtained when using special procedures like pilot holes or drilling paste.
- **Good** (***G***) – expected to work well, especially by optimizing standard process parameters like spindle speed and in-feed rate.

Most steels were rated *G*, but the *P* rating for TRIP 800 was based on the formation of flower-petal-like features at the exit sides of the holes.

Table 2. Assessment of ThD Response of Selected Alloys.

Alloy	Form and Stock Thickness (mm) (Note 1)	'Thermal Drillability' Rating
Al A380	DC (4.1)	*S P*
Al A319-T5	DC (4.1)	*S P*
Mg AZ91	DC (1.5, 3.0)	*M*
Mg AM60	DC (3.0)	*M*
Mg AE44	DC (3.0)	*M*
Mg AM50	DC (3.0)	*M*
DP 600 steel	Sh (1.2 – 2.2)	*G*
DP 780 steel	Sh (1.15 – 2.0)	*G*
Hydro-formed DP 780	HF (~ 2.5)	*G*
HSLA50 steel	Sh (1.14)	*G*
TRIP 800 steel	Sh (1.0)	*P*

Note 1) DC = die-cast, Sh = rolled sheet or plate

Spindle speeds and down-feed rates for the M6 hole-sized ThD tools are summarized in Table 3. It should be noted that the reported speeds and down-feeds were not optimized in this concept feasibility effort, but rather they were experimentally found to produce satisfactory holes for subsequent tapping and clamp-load testing.

Table 3. ThD Conditions for Alloys Used in this Project (M6 fastener holes).

Alloy	Spindle Speed (rpm)	Down-feed (in/min)
DP 600 steel	2500-4000	0.50
DP 780 steel	2000	0.75-1.00
HSLA50 steel	2000	0.50
Al A380*	10,000	2.5
Al A319-T5*	10,000	2.5
Mg AZ91D*	2,500	2.0
Mg AM60	8,000	2.0
Mg AE44*	8,000	2.0
Mg AM50	8,000	2.0

* Pilot holes were used.

Fastener Testing at PNNL

Torque-tension testing was performed at PNNL using the methods described in previous project reports.

The two primary factors that influence the clamp load at failure and the mode of failure are the thread-engagement depth of the fastener and the strength of the materials to be joined. For steel samples greater than 2-mm thick with either ThD and tapped holes and using the baseline design of 5- and 8-mm weld nuts and M6 machine screws, the failure mode was always to break the fastener and the clamp load at failure was 16-18 kN, as is shown in Figure 2. Similar performance was observed for ThD and tapped holes in DP 780 hydroformed tubes. Neither the type of steel nor the ThD process variables appeared to have an effect on the magnitude of clamp load.

For conventionally-drilled or thermally-drilled holes in steel plate with thicknesses of 1.5 mm or less, the failure mode was always stripping of the threads. Thermally drilled holes in 1.2 mm plates still generated nearly 14-16 kN in clamp load before stripping, whereas convention-ally drilled holes in the same thickness plate generated less than half that amount at ~7 kN.

For the lightweight aluminum and magnesium alloys, torque-tension testing of thermally drilled and tapped holes produced stripped threads at clamp loads of 6-8 kN. Further research is needed to optimize the microstructure and processing of lightweight alloys to achieve higher clamp loads.

Future Work

This project ended at the end of March 2007. Several car companies are considering the implementation of this novel production technology under internal sponsorship. Future R&D work is needed in several areas identified in the final report, particularly for non-ferrous alloys, but no follow-on effort has yet been identified.

Conclusions

The feasibility of thermally drilling a variety of ferrous and non-ferrous alloys, in various thicknesses, has been determined but not optimized. The success of this work was due in part to effective collaboration among USAMP team members and by the ability to draw upon prior work at the University of Michigan and ORNL. The following conclusions were reached:

1. High-strength steels, such as DP 600, DP 780, and HSLA50, seemed well suited for ThD, but TRIP 800 was not.
2. Thread-forming fasteners offer opportunities to make the best use of ThD technology and should be a focus for future work.
3. The formation of extended bushes by ThD can increase the tappable hole length in steel sheet products by as much as 300%.
4. ThD conditions must be developed for the specific material being drilled and cannot be generalized for all metals and alloys within a particular class (e.g., “steels”).
5. Maximum clamp-load data for thermally-drilled and tapped steel stock over 2.0-mm thick were encouraging and suggest the potential for using this method in assembling high-strength steel automotive components including hydroformed sections.
6. Additional research on the processing method is needed to improve the ThD results for aluminum and magnesium alloys which tend to have lower than desired maximum clamp loads.

A more extensive set of conclusions and a list of subjects for future research in thermal drilling are presented in the final report which is undergoing review.

Publications

1. P. J. Blau, B. C. Jolly, J. Qu, and D. M. Paxton (2007) *Feasibility of Thermally Drilling Automotive Alloy Sheet, Castings, and Hydroformed Shapes*, Final Project Report, to be published as an Oak Ridge National Laboratory Tech Report, 53 pp (under review).

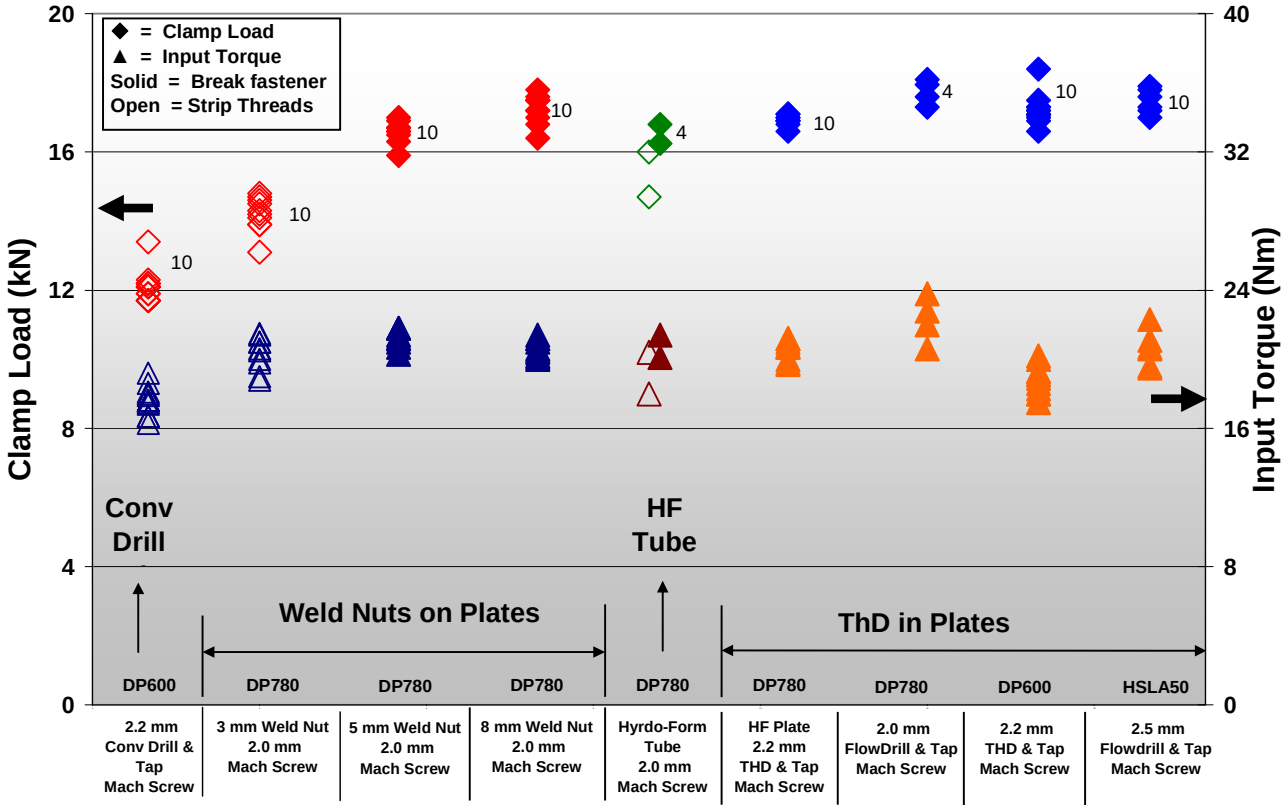

Figure 2. Torque-tension test results for ~2 mm thick steel samples with a variety of hole types and M6 machine screws with Magni 565 coating.

E. Weld-Element and Joining-Process Technology Development

Co-Principal Investigator: Douglas J. Bammann
Professor, Mechanical Engineering
Mississippi State University (MSST)
210 Carpenter Bldg.
Mississippi State, MS 39762
(662) 325-3260; Home: (662) 294-2585; e-mail: djb215@me.msstate.edu

Co-Principal Investigator: Sergio Felicelli
Associate Professor
MSST
Mechanical Engineering
Carpenter Engineering Bldg, Rm 210
Mississippi State, MS 39762
(662) 325-1201; e-mail: felicelli@me.msstate.edu

Postdoctoral Associate: Liang Wang
Center for Advanced Vehicular Systems (CAVS), 2182-B
MSST, P.O. Box 5405
Mississippi State, MS 39762-5405
(662) 325-9235; Home: (662) 325-5421; e-mail: liangw@cavs.msstate.edu

Co-Principal Investigator: Wing Kam Liu
Walter P. Murphy Professor of Mechanical Engineering
Director of the NSF Summer Institute on Nano Mechanics and Materials
Robert R. McCormick School of Engineering and Applied Science
Northwestern University (NU)
Department of Mechanical Engineering
2145 Sheridan Road
Evanston, Illinois 60208-3111
(847) 491-7094; fax: (847) 491-3915; e-mail: w-liu@northwestern.edu

Co-Principal Investigator: Ted Belyteschko
McCormick Professor of Computational Mechanics
Walter P. Murphy Professor of Computational Mechanics
Departments of Civil and Mechanical Engineering
Robert R. McCormick School of Engineering and Applied Science
NU
2145 Sheridan Road
Evanston, Illinois 60208-3111
(847) 491-7270; fax: (847) 491-3915; e-mail: tedbelytschko@northwestern.edu

Co-Principal Investigator: Michael Santella
Oak Ridge National Laboratory (ORNL)
1 Bethel Valley Road, Oak Ridge, TN 37831-6096
(865) 574-4805; fax: (865) 574-4928; e-mail: santellaml@ornl.gov

Co-Principal Investigator: Zhili Feng
ORNL
1 Bethel Valley Road, Oak Ridge, TN 37831
(865) 576-3797; fax: (865) 574-4928; e-mail: fengz@ornl.gov

Co-Principal Investigator: Srdjan Simunovic
ORNL
1 Bethel Valley Road, Oak Ridge TN 37831-6359
(865) 241-3863, fax: (865) 241-0381; e-mail: simunovics@ornl.gov

Technology Area Development Manager: Joseph A. Carpenter
(202) 586-1022; fax: (202) 586-1600; e-mail: joseph.carpenter@ee.doe.gov

Field Technical Monitor: Philip S. Sklad
(865) 574-5069; fax: (865) 574-6098; e-mail: skladps@ornl.gov

---

Contractor: MSST
Contract No.: 4000054701

Objective

- Develop the next generation of weld-element technology and joining-process technology (i.e., spot welding, ultrasonic welding) and assess the applicability of new technology for impact simulations and process optimization using lightweight alloys.

Approach

- Currently, weld-element performance and failure is based on a simple beam model in which the weld is modeled as a single element between two welded sheets and failure is postulated to occur when the tension or a moment exceed a certain specified threshold. This type of model does not reflect the thermo-mechanical details of the welding process and, consequently is unable to address variations in strength due to differences in weld-process parameters and the metallurgy of the materials being joined.
- To develop the next generation of weld-analysis technology in which details of the welding process and the metallurgy of the parent material are reflected in the behavior of the weld element, the physics of the resistance-welding process must be modeled in detail. The nature of the solidification process within the weld will be studied. The computed thermal history induced during the welding process will be used to predict microstructural evolution within the weld and adjacent material, thereby allowing prediction of the large mechanical-property gradients associated with the weld. The evolution of damage in the weld under subsequent high strain-rate loading will be studied with strain-rate-dependent constitutive models.
- The development of an ultrasonic welding process has remained largely empirical because the process is extremely complex due to friction-induced deformation and heat generation. We plan to assess the feasibility of developing a weld-element technology and a three-dimensional (3D) process model which will enable a better design of the ultrasonic welding process.

Accomplishments

- A thermo-metallurgical-mechanical model was developed to predict the temperature distribution, solid-phase transformation, and residual stress during the spot-welding process with the commercial finite element software SYSWELD. The TRIP model was reviewed and summarized.

Future Direction

- A comprehensive review of the weld elements for all types of welding procedures – year 1 (MSST).
- The detailed finite-element model (FEM) will first be developed and used to predict the strength of a spot weld under high strain-rate loading; recent development of weld-simulation technology at ORNL will be utilized by MSST team to expedite the weld-element development – year 1 (MSST, ORNL).

- For validation, experiments will be performed to measure the strength of spot-welded coupons under various high strain-rate loadings – years 1 and 2 (ORNL, MSST).
- Following this development and validation of the detailed FEM, a simple weld element will be developed which approximates the mechanical response of the detailed model under high strain-rate loading – year 2 (MSST, ORNL, NU).
- A neural network will potentially be employed within the weld-element development process in conjunction with physics-based, structure-property relations – year 2 (MSST).
- Pilot-scale, high strain-rates tests of large spot-welded components using ORNL high-rate tester to compare with modeling results – year 2 (ORNL, MSST).
- Assess the feasibility of modeling ultrasonic welding process and developing FEM element technology – year 2 (ORNL, MSST, NU). Note: ORNL's effort on this task is planned to be covered under related funding from a DOE program.

Introduction

Resistance spot welding (RSW) is a common joining process used in automotive manufacturing, with thousands of spot welds in a single vehicle. When simulating the behavior of a vehicle under crash conditions, the mechanical behavior of the spot welds under dynamic loading must be incorporated. Currently, spot welds are simulated using a weld element based on a simple beam theory; a next- generation, spot-weld element is needed in which details of the welding process and the metallurgy of the parent material are reflected. A FEM was developed to predict the process-properties relations in the RSW, which model will be implemented in the Spot Weld Element formulation.

Finite Element Modeling

A 3D FEM was developed to simulate the spot-welding process using the commercial code SYSWELD. The model was used to predict the temperature distribution, molten zone, volume fraction of each phase, and residual stress for two-sheet spot welding. Electrical-thermal, thermal-metallurgical, and thermo-metallurgical-mechanical analyses were considered in this model.

Electrical-Thermal Model

In RSW, the heat is generated within the material being joined by the resistance to the passage of a high current through the metal parts which are held under a pre-set pressure. Considering the Joule effect as an internal heat source, the electrical-thermal governing equation is presented as

$$\rho\frac{\partial H}{\partial t} - div(\lambda \cdot \mathbf{grad}T) - \mathbf{grad}V \cdot \sigma \cdot \mathbf{grad}V - Q = 0. \quad (1)$$

The electrical phenomena in the computational domain are assumed to be governed by the electrokinetic model for a frequency close to 50 Hz:

$$div(\sigma \cdot \mathbf{grad}V) = 0 \quad (2)$$

where T, V are the temperature and the scalar electrical potential, respectively. ρ, λ, H, and σ represent the density, the thermal conductivity, the enthalpy, and the electrical conductivity of the medium. The full coupling between electrical and thermal phenomena can be governed by the term $\mathbf{grad}V \cdot \sigma \cdot \mathbf{grad}V$ in the heat equation.

Thermal-Metallurgical Model

In this model, the metallurgical transformations are temperature dependent and accompanied by latent heat effects which modify temperature distribution. The thermal properties depend on the temperature and material phase. Based on the thermal history at each point in the resistance spot welding process, the phase transformations that may occur in the material are predicted using the semi-empirical models presented below. Different metallurgical phases, austenite, ferrite, bainite and martensite, are taken into account for this study. For the martensitic transformation, the Koistinen-Marburger law is used [Koistinen, 1959]:

$$p_m(T) = \bar{p}_m(1 - \exp(-b(M_s - T)))$$
$$\text{for} \quad T \le M_s \quad (3)$$

where $\overline{p}_m$ represents the volume fraction of martensite obtained at an infinite low temperature ($\overline{p}_m$ is frequently assimilated to 1). M_s is the martensite start temperature and b is the evolution coefficient of the transformation process, taken as 0.015 in this model [ASM, 2005].

For the phase transformations involving diffusion in steels (austenitic, ferritic, and bainitic transformations), under isothermal conditions, the Johnson-Mehl-Avrami law is used [SYSWELD, 2005]:

$$p(T,t) = \overline{p}(T)\left(1 - \exp\left(-\left(\frac{t}{\tau_R(T)}\right)^{n(T)}\right)\right) \qquad (4)$$

where $\overline{p}$ represents the phase proportion obtained after an infinite time at temperature T, τ_R is the delay time, and n is the exponent associated with the reaction rate. The parameters of the Johnson-Mehl-Avrami model were extracted from the continuous cooling transformation (CCT) diagram according to the cooling rate and were inserted in the FE code in a tabular form.

Thermometallurgical-Mechanical Model

Several types of interactions between thermal and mechanical analyses are considered including the thermal strains, the volume changes due to the transformations, the influence of the phases on the behavior law, and the plasticity induced by metallurgical transformations. In this study, flat-tip electrodes are used and the mechanical analysis can be uncoupled from the thermometallurgical analysis. The mechanical contact area is equal to the electrothermal contact area, which is assumed to be constant.

The total strain rate is partitioned as follows:

$$\dot{\varepsilon} = \dot{\varepsilon}_e + \dot{\varepsilon}_p + \dot{\varepsilon}_{tp} + \dot{\varepsilon}_{th} \qquad (5)$$

where $\dot{\varepsilon}_e$, $\dot{\varepsilon}_p$, $\dot{\varepsilon}_{tp}$, and $\dot{\varepsilon}_{th}$ are elastic strain rate, plastic strain rate, transformation plasticity, and thermal and metallurgical strain rate, respectively.

Results and Discussions

Two 0.01-mm, zinc-coated, low-carbon steel sheets are utilized in this study. The thickness of each sheet is 0.7 mm. The electrode radius is 3 mm. The current frequency is 50 Hz and the current intensity is 9.2 kA during 20 periods starting at 0.1 s. The force is 3100N during 30 periods staring at 0.1 s.

The temperature contour at the end of the current application (t = 0.3 s) in Figure 1 shows the molten zone. The molten-zone size is determined by the melting temperature (1450 °C). The effect of the current intensity on the temperature distributions has been investigated.

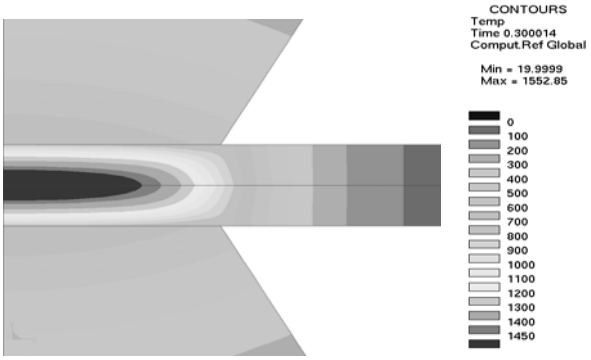

Figure 1. Temperature contour at the end of the current application (t = 0.3 s).

Figure 2 shows the temperature profiles at different locations along the interface between the two sheets with the current intensities of 9.2 kA and 12 kA. It can be seen that the local maximum temperature occurs on the left side of the interface between the two sheets and decreases along the interface. The maximum temperature is about 1500 °C for 9.2 kA, but it can reach 2200 °C for 12 kA on the left side of the interface. The molten zone increases with increasing current intensity.

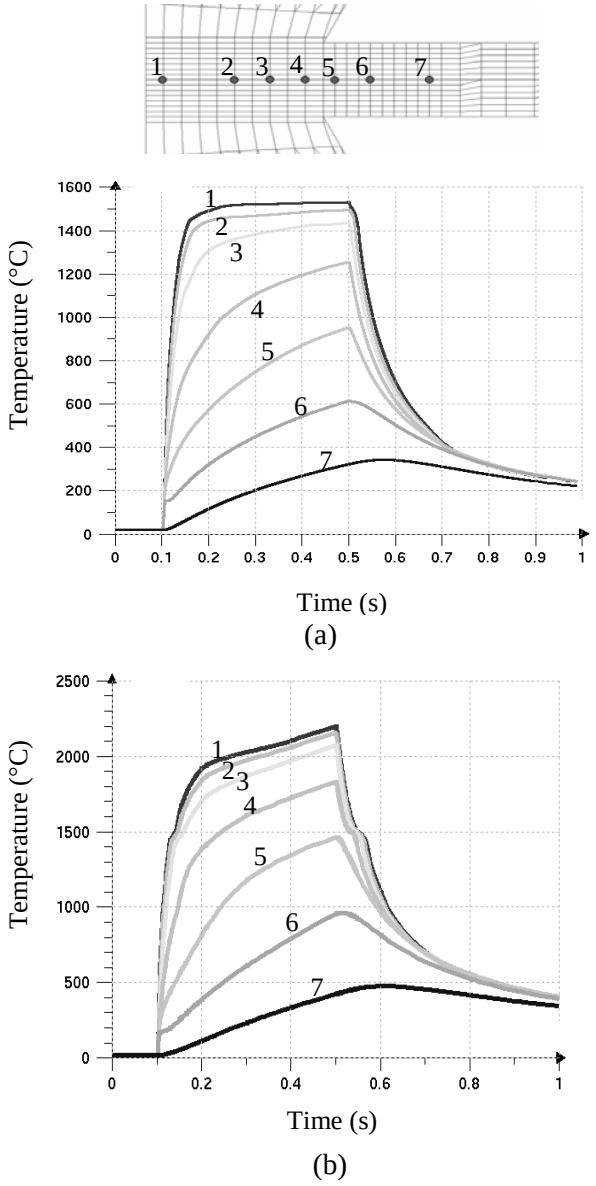

Figure 2. Temperature curves at different locations along the interface between two sheets at (a) 9.2 kA; (b) 12 kA.

Figure 3 shows the contours of ferritic and martensitic phase proportions at the end of the welding process. There are three types of zones. In the molten zone and around it, there is martensitic phase because it has been completely transformed. In a second zone, there is a mixture of the ferritic and martensitic phase. In the external zone, ferrite remains in the initial proportions since the base material was not heat affected.

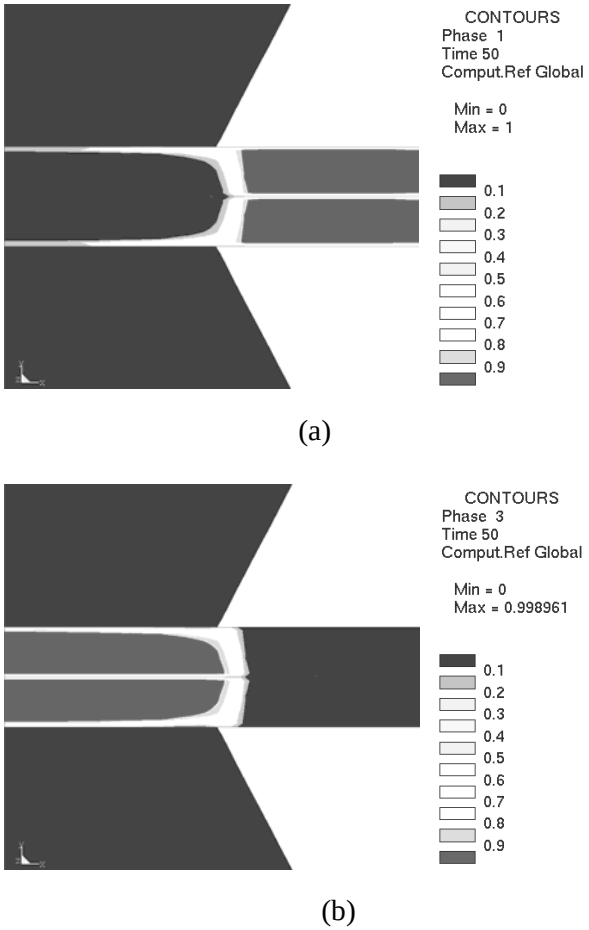

Figure 3. Volume fraction of (a) ferritic and (b) martensitic phase at the end of welding (t = 50 s).

The residual stresses, including Von Mises stress, in-plane stress (σ_{11}), and the stress perpendicular to the interface (σ_{33}), due to the welding process of the two sheets are presented in Figure 4. The most significant stresses are placed where the phases are the mixture of the ferritic and martensitic phases.

TRIP Model

As illustrated above, the model employed in SYSWELD can predict the residual stresses in resistance spot welding. However, in the presence of a deviatoric stress field, the weaker phase undergoes an additional deviatoric straining imposed upon it by the stronger phase. This transformation-induced plasticity (TRIP) can have substantial effects on residual stresses and

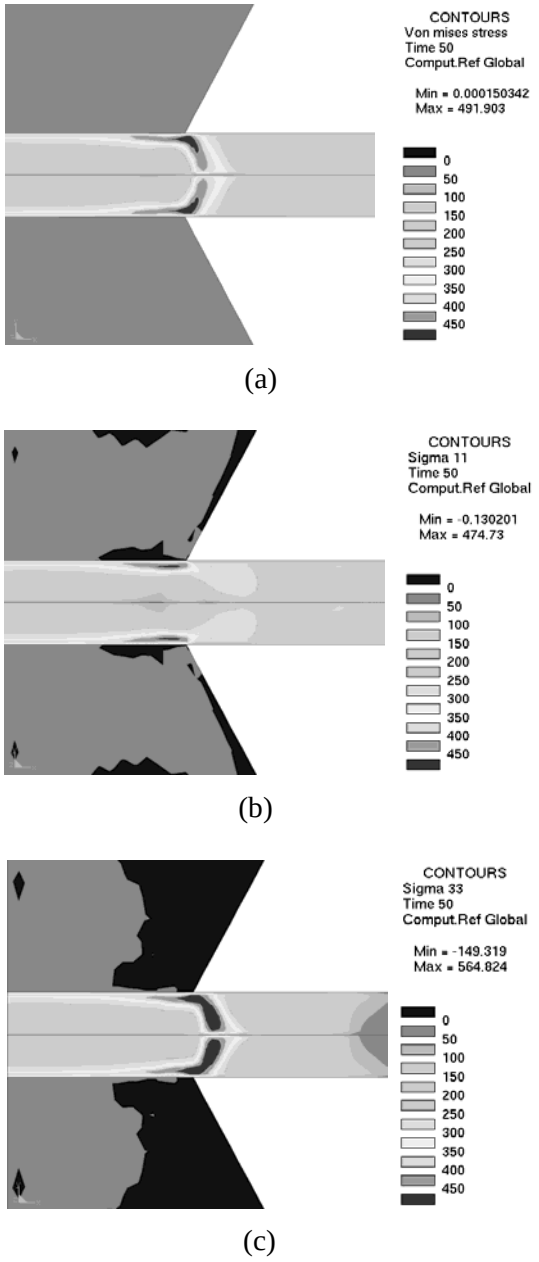

Figure 4. Residual stress distributions at the end of welding. (a) Von Mises stress, (b) $\sigma 11$, (c) $\sigma 33$.

distortions. Rather than utilizing existing empirical models to describe the TRIP effect, such as those employed in SYSWELD, we extend a single-phase, rate- and temperature-dependent, internal state variable model to describe multiple phases.

The model to be utilized in the description of the material response during the spot-welding process is an extension of a multiphase model developed previously to predict distortions and residual stresses in the heat-treatment and quenching process [Bammann, 1996]. To simplify the description, we consider only a two-phase model, although the following is easily generalized to five or more phases. We begin by including two features at the microscopic level that have direct effects on the macroscopic response for materials susceptible to phase transformations during rapid cooling. The volume difference associated with the phase change imparts a purely dilatational deformation. The volumetric strain associated with the phase change is included directly in the flow rule, while the TRIP effect is included by the introduction of interface stresses between the phases – the harder phase exerting a forward stress on the softer phase and a backward stress for the softer phase upon the harder one. An overview of this approach for two phases follows.

Internal state variable models have been utilized previously to describe the response of single-phase metals over large strain-rate and temperature ranges. These models have been formulated in a manner consistent with the kinematics of large-deformation, elastic-plastic response and are discussed elsewhere [Bammann, 1990]. For multiphase materials, additional complications arise in predicting the material response. In particular, the effects of phase-transformation-induced plastic strain must be included. As steel is cooled from above the austenization temperature, a solid-state phase transformation occurs, the detailed nature of which phase forms depending upon the temperature and the cooling rate. Although we consider only martensite here, the model is easily generalized to consider additional product phases. The martensite occupies approximately 4% more volume than the austenite from which it transforms. The yield strength of martensite can also be an order of magnitude higher than that for austenite. As the austenite transforms to martensite, a volumetric strain develops in the austenite owing to the volume mismatch and difference in strength. In the presence of any deviatoric far-field stress, this will be accompanied by a deviatoric component of strain. Since the martensite is much stronger, this results in a forward stress, $\pi^{(1)}$, in the austenite, resulting in an apparent softening of the material.

Similarly, a backward stress, $\pi^{(2)}$, is created in the martensite. This stress field is a true, tensorial backstress that must be subtracted from the applied stress to get the glide resistance to macroscopic plastic flow. To first order, it is proportional to the volume fraction of hard particles and has its microscopic origins in the TRIP mechanism [Kocks, 1987]. Introducing such a backstress in the yield condition and flow rule provides a natural way to model the apparent yield drop and additional plasticity characteristic of TRIP.

To generalize the state-variable model for multiphase materials, we assume that each point of the continuum can be occupied simultaneously by all phases. Each phase is modeled by the appropriate state-variable model for that phase with rate and temperature dependence as described in [Bammann, 1990]. The material response can then be modeled with as much complexity or simplicity as required, since the model reduces to rate-independent, bilinear response with an appropriate choice of parameters. We denote the current configuration deviatoric Cauchy stress in the austenite and martensite by $\sigma'^{(1)}$ and $\sigma'^{(2)}$, respectively. We assume a classic volume-fraction-weighted rule of mixtures, such that the total Cauchy stress, σ', is given by

$$\sigma' = \Phi\sigma'^{(2)} + (1-\Phi)\sigma'^{(1)} \tag{6}$$

We assume a hypoelastic relation for each phase that is consistent with an assumption of linear elasticity giving

$$\overset{\circ}{\sigma}'^{(i)} = 2\mu D'^{(i)}_e + \frac{\dot{\mu}}{\mu}\sigma'^{(i)} \tag{7}$$

where $D'^{(i)}_e$ is the elastic symmetric part of the deviatoric velocity gradient, and μ is the temperature-dependent shear modulus, assumed to be the same for both phases. Elastic-deformation rates are defined as the difference between the total deformation rate and the sum of the thermal, $D'^{(i)}_{th}$, and the inelastic, $D'^{(i)}_p$, contributions in each phase

$$D'^{(i)}_e = D' - D'^{(i)}_p - D'^{(i)}_{th} \tag{8}$$

Here, $\circ$ denotes the convective derivative of the Cauchy stress defined by

$$\overset{\circ}{\sigma}^{(i)} = \dot{\sigma}^{(i)} - W_e^{(i)}\sigma^{(i)} + \sigma^{(i)}W_e^{(i)} \tag{9}$$

where $W_e^{(i)}$ is the skew part of the elastic velocity gradient for each respective phase given by

$$W_e^{(i)} = W - W_p^{(i)} \tag{10}$$

For the present purposes, we choose a Jaumann derivative and all $W_p = 0$. Defining, $\pi^{(2)}$ and $\pi^{(1)}$ as the backward and forward long-range stresses in the martensite and austenite, respectively,

$$\pi^{(2)} = \frac{-(1-\Phi)}{\Phi}\pi^{(1)} \tag{11}$$

This type of approach was taken by Freed, Raj and Walker [Freed, 1992] in modeling the hard and soft regions of a polycrystalline material as first proposed by Kocks [Kocks, 1987].

Approximating compatibility of the hard and soft regions using the self-consistent scheme of Budiansky and Wu [Budiansky, 1962], they found that the total and local deviatoric strain fields must satisfy

$$\varepsilon'^{(i)} = \varepsilon' + \left(\frac{\beta}{1-\beta}\right)\frac{\pi^{(j)}}{2\mu} \tag{12}$$

where i, j=1,2 and i is not equal to j. Here, β is the Eshelby shape factor for a spherical inclusion. We will make a simplifying Taylor-like assumption and assume that the strains in each field are identical. In an effort to relieve this assumption, a numerical micromechanical simulation of the deformation partitioning will be the subject of a future work.

In addition to the long-range forward and backward internal stress fields which act between the phases, we assume the existence of two short-range internal stress fields, $\alpha^{(i)}$ and $\kappa^{(i)}$, which

act locally within each phase. We then define the net stress acting in each phase as

$$\xi^{(i)} = \sigma'^{(i)} - \alpha^{(i)} - \kappa^{(i)} - \pi^{(i)} \tag{13}$$

Now, we impose specific assumptions concerning the directionality of the stresses $\pi^{(i)}$ and $\kappa^{(i)}$. In particular, we postulate that they act in the direction of the Cauchy stress minus the short-range stress, $\alpha^{(i)}$, in each phase,

$$\pi^{(i)} = \pi^{(i)} \frac{\sigma'^{(i)} - \alpha^{(i)}}{\left|\sigma'^{(i)} - \alpha^{(i)}\right|} \quad \kappa^{(i)} = \kappa^{(i)} \frac{\sigma'^{(i)} - \alpha^{(i)}}{\left|\sigma'^{(i)} - \alpha^{(i)}\right|} \tag{14}$$

The effective stresses acting to cause plastic flow in each phase are then given by

$$\left|\xi^{(i)}\right| = \left|\sigma'^{(i)} - \alpha^{(i)}\right| - \kappa^{(i)} - \pi^{(i)} \tag{15}$$

where $\kappa^{(i)}$ are the scalar internal variables acting in each phase as discussed above. The plastic flow rule is chosen to have a strong nonlinear dependence upon the deviatoric stress

$$D_P^{(i)} = f^{(i)}(\theta) \sinh\left\{\frac{\xi^{(i)} - Y^{(i)}(\theta)}{V^{(i)}(\theta)(1 + N(c))}\right\} \frac{\sigma'^{(i)} - \alpha^{(i)}}{\left|\sigma'^{(i)} - \alpha^{(i)}\right|} \tag{16}$$

where $f(\theta)$ and $V(\theta)$ describe a rate dependence of the yield stress at constant temperature and N(c) describes the yield increase with increasing carbon content, c. Tensor variables, $\alpha^{(i)}$, and scalar variables, $\kappa^{(i)}$, have been introduced to describe the deformed state of each phase as described previously for a single phase material [Kocks, 1987]. The evolution of these variables is defined for phase (i) by

$$\begin{aligned} \dot{\kappa}^{(i)} &= H^{(i)}(\theta, c)\left|D_P^{(i)}\right| - \left\{R_S^{(i)}(\theta) + R_D^{(i)}(\theta)\left|D_P^{(i)}\right|\right\}\kappa^{(i)}\left|\kappa^{(i)}\right| \\ \dot{\alpha}^{(i)} &= h^{(i)}(\theta, c) D_P^{(i)} - \left\{r_S^{(i)}(\theta) + r_D^{(i)}(\theta)\left|D_P^{(i)}\right|\right\}\alpha^{(i)}\left|\alpha^{(i)}\right| \end{aligned} \tag{17}$$

The fit to the carbon-dependent data reported by Sjöström [Sjöström, 1982] is shown in Figure 5. Finally, we adopt the simplest evolution equation for the long-range internal stress that is, to first order, proportional to volume fraction, but vanishes as the austenite transforms entirely to martensite

$$\dot{\pi} = C \frac{\Delta V}{V}\left\{\dot{\Phi} - 2\Phi\dot{\Phi}\right\} \tag{18}$$

Here, a simple exponential kinetics are used as described in [Lusk, 1995]

$$\dot{\Phi} = \tilde{k} \exp\left(\lambda_j \left\{\eta - \eta_M\right\}^2\right)\dot{\eta}; \; j = 1,2 \tag{19}$$

where η is the driving force for transformation,

$$\eta = k(M_s - \theta) \tag{20}$$

and M_s is the martensite start temperature. Here, λ_{12} and η_M are prescribed by the rate kinetics [Oddy, 1990].

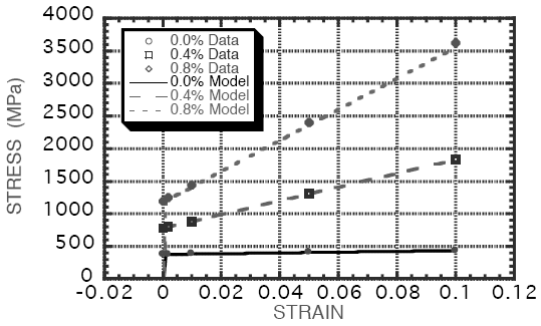

Figure 5. Stress-strain curves to fit the carbon dependent data [Sjöström, 1982].

This model has been extended successfully to account for five phases and utilized in finite-element description of the quenching of a gear blank. In this analysis, a fundamental balance principle was used to model phase-transformation kinetics at a volume-fraction level for a broad range of industrial steels. This micro balance provides differential equations for transformation kinetics which couple naturally to the differential equations governing the mechanical and thermal aspects of a given process [Fried, 1994, Fried, 1993]. Avrami-type kinetics, as well as the Koistinen-Marburger equation, have been shown to result from special classes of energy and mobility functions [Lusk, 1995]. An illustrative example using a 5140 alloy demonstrates how Time-Temperature-Transformation (TTT) and

Continuous Cooling Transformation (CCT) curves can be generated using a particularly simple energy function. The formulation of this theory is discussed in [Lusk, 1995] for a single product phase, and in modeling the possibly competitive development of ferrite, pearlite, bainite and martensite. This model will be applied to the spot-weld problem. Extensions to the model will include more accurate distributions of the strain among the phases using a combination of statistical mechanics and self-consistent scheme. Also, more physical descriptions of the flow rule and state variable evolution for the non-austenite phases will be addressed.

Conclusions

A finite-element model was developed to predict the thermal behavior, molten zone, solid phase transformation and the residual stress during the resistance spot welding. The calculation was performed with the commercial software SYSWELD. Preliminary study on the effects of process parameter (current intensity) on the temperature distribution and molten zone was performed. The results show that SYSWELD is an effective tool to perform numerical modeling in the resistance spot welding process in order to determine the process-properties relations.

A framework of phase-transformation kinetics based on TRIP concepts was presented. This will enhance the development of welding-modeling work with robust materials models for weld and weld-effective zones, in which critical experiments will be guided by the needs of models rather than by empirical approaches.

Presentations/Publications/Patents

None.

References

1. [Koistinen, 1959] D. P. Koistinen and R. E. Marburger, A General Equation Prescribing the Extent of Austenite-Martensite Transformation in Pure Fe-C Alloys and Plain Carbon Steels, Acta Metall., vol. 7, pp. 417–426, 1959.
2. [ASM, 2005] ASM Handbook, Welding, Brazing, and Soldering, Vol. 6, ASM International, Material Park, OH, 2005, 438.
3. [SYSWELD, 2005] SYSWELD 2005 Reference Manual, ESI Group, 2005.
4. [Bammann, 1996] Bammann, D. J., Prantil, V. C., Kumar, A., Lathrop, J., Mosher, D., Callabresi, M., Lusk, M., Krauss, G., Jou, H. J., Elliott, W., Ludtka, G., Dowling, W., Nikkel, D., Lowe, T., Shick, D., "Development of a Carburizing and Quenching Simulation Tool: A Material Model for Carburizing Steels Undergoing Phase Transformations," *2nd Int. Conf. on Quenching and the Control of Distortion*, Cleveland, OH, 1996.
5. [Bammann, 1990] D. J. Bammann, "Modeling Temperature and Strain Rate Dependent Large of Metals," *Applied Mechanics Reviews*, Vol. 43, No. 5, Part 2, May, 1990.
6. [Kocks, 1987] U. F. Kocks, "Constitutive Behavior Based on Crystal Plasticity," *Unified Constitutive Equations for Creep and Plasticity*, ed. A. Miller (London: Elsevier Applied Science, 1987), 1-88.
7. [Freed, 1992] A. D. Freed, S. V. Raj, and K. P. Walker, "Three-Dimensional Deformation Analysis of Two-Phase Dislocation Substructures," *Metallurgica et. Materialia*, 27 (1992), 233-238.
8. [Budiansky, 1962] B. Budiansky and T. T. Wu, "Theoretical Prediction of Plastic Strains of Polycrystals," *Proc. Fourth U. S. Cong. Appl. Mech.*, Vol. 2, (New York, NY: American Society of Mechanical Engineers, 1962), 1175-1185
9. [Sjöström, 1982] S. Sjöström, "The Calculation of Quench Stresses in Steel," (*Ph.D. Thesis, Linkoping University, Sweden, 1982).*
10. [Lusk, 1995] Lusk, M., Krauss, G., and H.-J. Jou, *Journal de Physique IV*, C8 (1995) 279-284.
11. [Oddy, 1990] A.S. Oddy, J.A. Goldak, and J.M.J. McDill, "Numerical Analysis of Transformation Plasticity in 3D Finite Element Analysis of Welds," *Eur. J. Mech., A/Solids*, 9 (3) (1990), 253-263.

12. [Fried, 1994] Fried, E. and Gurtin, M., *Phys. D*, 72 (1994) 287-308.
13. [Fried, 1993] Fried, E. and Gurtin, M., *Phys. D*, 68 (1993) 326-343.